Escape rate calculations for active Brownian particles with non-Gaussian noise

A Thesis

Submitted to

Indian Institute of Science Education and Research Pune in partial fulfilment of the requirements for the BS-MS Dual Degree Programme

by

C Karthik

IISER PUNE

Indian Institute of Science Education and Research Pune
Dr. Homi Bhabha Road,
Pashan, Pune 411008, INDIA.

April, 2025
Supervisor: Prof. Dr. Peter Sollich
C Karthik

CERTIFICATE

This is to certify that this dissertation entitled “Escape rate calculations for active Brownian particles with non-Gaussian noise” towards the partial fulfilment of the BS-MS dual degree programme at the Indian Institute of Science Education and Research, Pune represents study/work carried out by C Karthik at Georg-August-Universität Göttingen under the supervision of Prof. Dr. Peter Sollich, Institute for Theoretical Physics during the academic year 2024.

Peter

Signature of Supervisor

Karth

Signature of Student

Declaration

I hereby declare that the matter embodied in the report entitled "Escape rate calculations for active Brownian particles with non-Gaussian noise" are the results of the work carried out by me at the Department of theoretical physics, Georg-August-Universität Göttingen, under the supervision of Prof. Dr. Peter Sollich and the same has not been submitted elsewhere for any other degree.

karth

Signature of Student

Acknowledgements

I would like to thank Prof. Peter Sollich for giving me the opportunity to work on this project. This work was done in collaboration with Dr. Rafael Díaz Hernández Rojas. His help was crucial both in independent verification of several results and in insightful discussions and suggestions on the project. The present work is a continuation of research by Dr. Diego Tapias and Leif Peters.

I would also like to thank my family for their unconditional support - both financial and emotional - at every step of the way.

Abstract

We study the escape behavior of Run and Tumble particles from confining potentials in the presence of non-Gaussian noise using the MSR path integral formalism. We define a weak noise limit and find the most probable escape path by solving the corresponding Hamilton's equations and by path based optimization using the Geometric Minimum Action method. We find that the escape rate is enhanced exponentially with non-Gaussian noise. It is seen that even in the weak noise limit, the optimal escape path shows run and tumble behavior for some types of non-Gaussian noise. Finally, we briefly describe an activity induced phase transition.

Contents

List of Figures

Chapter 1

Introduction

Modelling physical phenomena with stochastic dynamics is a practice that has proved successful in a wide variety of fields, from neuroscience to chemical physics. Broadly speaking, the aim of stochastic modelling is to capture the effect of degrees of freedom that are too numerous or complex to be described and controlled using random variables. These might be external interactions like a tracer interacting with particles of its fluid medium or internal degrees of freedom like individuals in a population.

A particular example of a stochastic system that will be considered in this thesis is the Active Brownian Particle(ABP). First studied by the biologist Robert Brown and later by Albert Einstein and Paul Langevin, Brownian particles describe the motion of a passive mesoscopic particle due to collisions with a fluid medium. This is essentially an equilibrium system which is insufficient to explain the far from equilibrium phenomena seen in nature, for example living systems like the cell. In addition to random collisions, an active particle has internal sources of energy it uses to move with a self-propulsion, breaking detailed balance[1]. The exact mechanism of this self propulsion could be due to hydrodynamic effects resulting from non-reciprocal motion of cilia/flagella in a bacterium or chemical reactions that happen inhomogeneously over the surface of a reactant, but the net effect is that the particle has an orientation defined by the direction in which it would move by aid of this self propulsion in the absence of the thermal medium. This orientation is also affected by noise, either due to interaction with the medium or internal details that are abstracted as noise. In the context of ABPs, this is usually Gaussian. However with the addition of non-Gaussian noise in self propulsion, we can model the run and tumble motion that is widely seen in nature where instead of continuous noise the orientation remains constant during "run" phases between intermittent "tumble" phases where it is changed rapidly. These are called Run and Tumble Particles(RTPs)[2].

Active Matter (both individually and collectively) show a variety of novel behaviors like wall accumulation and motility induced phase separation[3][4] that is not seen in equilibrium. We are interested in describing the escape behaviour of a single ABP from a confining potential. Kramers showed that a Brownian particle in a potential of depth ΔV will escape at a rate $C \exp\left(-\frac{\Delta V}{k_b T}\right)$ where C is a constant[5]. C is dependant on the specifics of the model, but the exponential dependence is very general. This allows us to define metastability where the particle spends most of its time in a metastable state with rare noise-assisted transitions to other stable or metastable states. These rare transitions explain chemical reaction systems, phase slip in mode-locked lasers, rare extinction events in populations and disease spread[6]

To extend the Kramers result to ABPs and RTPs, there are a few avenues of approach. In 1-d, exact expressions for the mean first passage time of RTPs can be obtained by solving the Fokker-Plank equation[7]. In 2-dimensions, there are exact results of the positional density for simple tumble noise strength (uniform or discrete) in the absence of a potential[8] and numerical results using transition path sampling[9]. For ABPs, there are analytical expressions in some limits of noise strength[10]. There are also exact solutions for simple potentials that confine motion in one direction[11] via solving the Fokker-Plank equation. Another approach has been to make an effective equilibrium approximation[12] where the angular noise is approximated with an Ornstein-Uhlenbeck process. Numerical simulation of these barrier crossings are hard because escape trajectories occur rarely. There are ways to get around this by using specialized sampling techniques like the aforementioned transition path sampling or forward flux sampling[13].

We will use a path integral approach to tackle this problem. An advantage of this approach is that it can take into account both Gaussian and non-Gaussian noise i.e.both active and run and tumble behavior simultaneously even when they are of comparable strength. Additionally, the magnitude of self propulsion change after a tumble can be very general. The problem of noise-activated escape with shot noise was considered in [14]. Escape rates of ABPs from an elliptic potential was studied in [15]. This thesis is an attempt to extend their results to study the effect of non-Gaussian noise acting indirectly via the self propulsion of an ABP.

1.1 The model particle

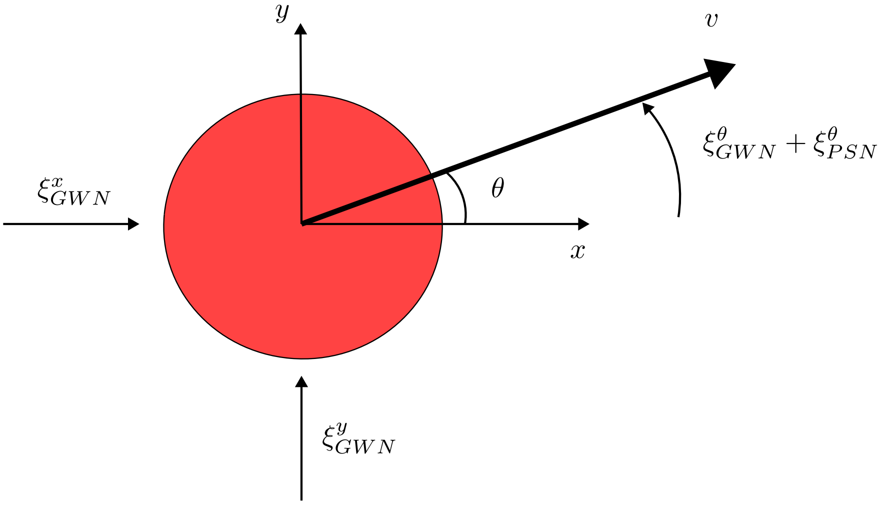

Figure 1.1: Schematic representation of the model particle

The equations of motion the model particle are as follows

$$\dot{x} = -\partial_x V + v\cos\theta + \xi^{x}_{GWN} \tag{1.1}$$

$$\dot{y} = -\partial_y V + v\sin\theta + \xi^{y}_{GWN} \tag{1.2}$$

$$\dot{\theta} = \xi^{\theta}_{GWN} + \xi^{\theta}_{PSN} \tag{1.3}$$

We assume that ξ^{x}_{GWN}, ξ^{y}_{GWN} and ξ^{θ}_{GWN} are independent Gaussian White Noise(GWN) of strength D for the spatial and D_θ for the angular components respectively, meaning they are Gaussian distributed for a fixed time and are δ corellated across different times.

$$\langle \xi^{x}_{GWN}(t)\xi^{x}_{GWN}(t')\rangle = \tilde{D}\delta(t-t') \tag{1.4}$$

$$\langle \xi^{y}_{GWN}(t)\xi^{y}_{GWN}(t')\rangle = \tilde{D}\delta(t-t') \tag{1.5}$$

$$\left\langle \xi^{\theta}_{GWN}(t)\xi^{\theta}_{GWN}(t')\right\rangle = \tilde{D}_\theta\delta(t-t') \tag{1.6}$$

We model the run and tumble behavior using memoryless Poisson Shot Noise (PSN). In the equation of motion, this is present as the term ξ^{θ}_{PSN}. The particle experiences intermittent kicks (tumbles) such that the inter-kick time interval is independent of the kick history and distributed exponentially with a parameter $\tilde{\lambda}$. The magnitude of the kick is constructed from a baseline distribution ρ. We set ρ to have unit variance (but do not insist on it being normalizable). From this, the probability density of the kick magnitudes are defined to be

$$\rho_{PSN}(x) = \frac{1}{\tilde{a}}\rho\left(\frac{x}{\tilde{a}}\right) \tag{1.7}$$

This allows us to control the typical tumble magnitude, since the variance of $\rho_{PSN}(x)$ is $\tilde{a}^2$. The exact types of ρ used will be discussed in the next section. The PSN can describe a wide range of run and tumble behaviors.

For convenience, we will refer to the model as an ABP even when $\tilde{\lambda} \neq 0$. To refer to the usual scenario with $\tilde{\lambda} = 0$, we will specify that the particle is only experiencing GWN. To simplify notation, $\mathbf{r}$ will denote (x, y) and $\mathbf{q}$ will denote (x, y, θ).

1.2 Barrier crossing

Our aim will be to find relative probabilities for different transition paths thus the most probable one. Since the only randomness in the system is due to noise, the probability of a path can be translated into the probability of a particular noise history. This can be written in the form

$$\mathbb{P}[\mathbf{q}, \dot{\mathbf{q}}] \propto \exp\left(\frac{-S(\mathbf{q}, \dot{\mathbf{q}})}{\varepsilon}\right) \tag{1.8}$$

where S is a functional of the path and ε depends on the noise strength. The proportionality constant is sub-exponential. Any deviation from a minimum of S is exponentially suppressed and for small ε, it is negligible. This idea is formalized by the theory of large deviations[16]. In slightly more precise terms,

$$\lim_{\varepsilon \to 0} -\varepsilon \ln \mathbb{P}_{\varepsilon}[\mathbf{q}, \dot{\mathbf{q}}] = S(\mathbf{q}, \dot{\mathbf{q}}) \tag{1.9}$$

Here, $\mathbb{P}_{\varepsilon}$ is the trajectory distribution with noise strength ε and $\lim_{\varepsilon \to 0} \mathbb{P}_{\varepsilon} = \mathbb{P}$ is said to follow a large deviation principle with rate (or law) S. The large deviation principle of a passive Brownian particle is well known and studied as a part of Freidlin-Wentzell theory[17]. For passive diffusion, S can be expressed as the integral of an instantaneous Lagrangian. An example of a Langevin equation and its Lagrangian is given below. This can be generalized to higher dimensions and multiplicative noise. In (1.10), ξ is GWN of unit variance.

$$\dot{x} = -\partial_x V(x) + \sqrt{\varepsilon}\xi(t) \tag{1.10}$$

$$S = \frac{1}{2} \int_0^{t_f} \underbrace{(\partial_x V(x) - \dot{x})^2 \, \mathrm{d}t}_{\mathcal{L}} \tag{1.11}$$

For the case of an ABP, we use the Martin-Siggia-Rose(MSR) path integral formalism. It must be noted that the original MSR method was operator based and rather complicated. The current methodology using path integrals is by De Dominicis, Peliti and Janssen. It is therefore sometimes called the MSR-DPJ formalism[18]. As before, we define the weak noise by taking the variances of the noises to zero so that the path probability density is sharply peaked about the most probable value.

$$\tilde{D} = \varepsilon D \qquad \tilde{D}_\theta = \varepsilon D_\theta \qquad \tilde{\lambda} = \frac{\lambda}{\varepsilon} \qquad \tilde{a} = \varepsilon a \tag{1.12}$$

with $\varepsilon \to 0$. Since the variance of shot noise is $\tilde{\lambda}\tilde{a}^2$, the strength of the non-Gaussian noise goes to zero also. The reason for this choice of a weak noise limit is discussed in Appendix A. For an ABP, the path probabilities are of the form

$$\mathbf{P}[\mathbf{q}, \dot{\mathbf{q}}] \propto \exp\left(\frac{-1}{\varepsilon}\int_0^{t_f}\left[\max_{\mathbf{k}} \dot{\mathbf{q}}(s)\cdot\mathbf{k} - \mathcal{H}(\mathbf{q}(s), \mathbf{k}(s))\right]\mathrm{d}s\right) \tag{1.13}$$

where

$$\mathcal{H}(\mathbf{q}, \mathbf{k}) = (v\cos\theta - \partial_x V)k_x + (v\sin\theta - \partial_y V)k_y + \lambda\phi(ak_\theta) + \frac{D}{2}(k_x^2 + k_y^2) + \frac{D_\theta}{2}k_\theta^2 \tag{1.14}$$

Here, ϕ contains all information about the shot noise. ϕ is related to the moment generating function of ρ as

$$\phi(x) = \int_{-\infty}^{\infty}\left(e^{xu} - 1\right)\rho(u)\mathrm{d}u \tag{1.15}$$

Thus even with non-Gaussian noise and activity, we have the law being an integral over an instantaneous Lagrangian. However we do not have the Lagrangian directly - it is only present as the Legendre transform of a Hamiltonian $\mathcal{H}$. In general, this Legendre transform can not be computed analytically for $\lambda > 0$. Details about the derivation of the MSR action can be found in Appendix A. $\mathbf{k}$, the momenta conjugate to $\mathbf{q}$, can be interpreted as the magnitude of fluctuations needed for a path. Since only the values of D_θ, D, λ relative to each other matter in (1.14), we will always set $D = 1$

The particle will be in a confining potential at an initial position $\mathbf{r}_i$. It will be considered escaped if it reaches some $\mathbf{r}_f$. The potential landscape is such that for any path $\mathbf{r}(t)$ between the initial and final points, $\nabla_{\mathbf{r}}V(\mathbf{r}(t))\cdot(\mathbf{r} - \mathbf{r}_i) > 0$ for at least some portion of the path. We do not fix θ at the initial and escape points as it is usually not controllable. This is somewhat stricter than realistic escape scenarios where it is sufficient for the particle to cross some region of space where there is an upward potential gradient and the final point too is not fixed[19]. Since θ is not fixed at the ends the boundary condition corresponding to stationarity in θ is that $k_\theta = 0$. For a fixed t_f, finding the most probable escape path is now a variational problem to minimize the action. For smooth trajectories, this is equivalent to solving the 6 Hamilton's equations we get from (1.14). Fixing $\mathbf{r}$ and k_θ at both ends give us enough boundary conditions to get a unique solution.

To find the most probable escape path, we also should not fix t_f. For escape paths that pass through a fixed point of the noiseless dynamics, it is generally true that the action decreases with increasing t_f before saturating. Intuitively, this is because the particle can "wait" at the fixed point for arbitrarily long periods of time for the optimal rare fluctuation that takes it to the escape point. In all the potentials we look at, every possible escape trajectory will pass through a fixed point. Thus we are interested in finding

$$\lim_{t_f \to \infty} \arg\min_{\mathbf{q}, \dot{\mathbf{q}}} S_{t_f}(\mathbf{q}, \dot{\mathbf{q}}) \tag{1.16}$$

It must be noted that while the Hamilton's equations assume smooth trajectories, the action can take discontinuous or non-differentiable trajectories as inputs also. This is done by first taking the weak noise limit for a discretized version of (1.13) and then reducing the discretization spacing to 0. This point is of physical concern. As we will see in the next section, for some noise distributions ρ, the optimal escape path can indeed be discontinuous.

1.3 Escape in one dimension

To compare the effects of non-Gaussian noise on the self propulsion angle versus the position of a Brownian particle, we state the main results of [14] and explain in brief the methods used to derive. This is because in 1-D, analytical results are tractable and a lot of our intuition for the problem at hand stems from these. The classification of noise types will also be relevant for the ABP.

Since the noise acts directly on the particle, its equation of motion is of the form

$$\dot{q} = -\partial_q V(q) + \xi_{GWN} + \xi_{PSN} \tag{1.17}$$

and the particle moves from an initial point q_i to a final point $q_f > q_i$. By a process very similar to the derivation in Appendix A, the Lagrangian for this system is of the form

$$\mathcal{L} = \max_k k(\dot{q} + \partial_q V) - \underbrace{\left(\frac{Dk^2}{2} + \lambda \phi(ak) \right)}_{\psi(k)} \tag{1.18}$$

The momentum k^* which maximizes the expression above satisfies $\dot{q} + \partial_q V = \psi'(k^*)$. To sidestep the minimization in time, a path length reparametrization is done with $s(t) = \int_0^t |\dot{q}| \mathrm{d}t$. Note that $\dot{q} > 0$ since the particle has to move in the +ve direction to escape and its unlikely that a move in the opposite direction will result in a lower total action. In 1-d, the only possible path is a straight line (assume there is no self intersection). Thus, the action minimization is

$$S_{\text{min}} = \min_{\dot{q}} \int_{q_i}^{q_f} \frac{\mathcal{L}(q,\dot{q})}{\dot{q}} \mathrm{d}q \tag{1.19}$$

A point wise minimization in $\dot{q}$ is done. Assuming the minimum occurs at finite $\dot{q}$,this means that $\frac{\mathrm{d}}{\mathrm{d}\dot{q}}\left(\frac{\mathcal{L}}{\dot{q}}\right) = 0$. Expanding the derivatives,

$$\begin{align}
\frac{\mathcal{L}}{\dot{q}} &= \frac{\mathrm{d}\mathcal{L}}{\mathrm{d}\dot{q}} \tag{1.20}\\
&= (\dot{q} + \partial_q V)\partial_{\dot{q}} k^* + k^* - \psi'(k^*)\partial_{\dot{q}} k^* \tag{1.21}\\
&= \partial_{\dot{q}} k^* [\dot{q} + \partial_q V - \psi'(k^*)] + k^* \tag{1.22}\\
&= k^* \tag{1.23}
\end{align}$$

We have used the maximization condition in k^* to get (1.23). Using the definition of the Lagrangian in (1.18) we proceed to get

$$\partial_q V = \frac{\psi(k^*)}{k^*} = \frac{Dk^*}{2} + \lambda \frac{\phi(ak^*)}{k^*} \tag{1.24}$$

Since we now have k^* in terms of q by solving (1.24), the minimum action path obtained by minimization over $\dot{q}$ and t_f has an action $\int_{q_i}^{q_f} k^*(V'(q))$.

In particular, setting $\lambda = 0$ gives $k^* = \frac{2}{D}\partial_q V$ and so $S = \frac{2\Delta V}{D}$ which is the Kramers result. The non-Gaussian effects are basically due to deviations of k^* from the Gaussian value. Since ϕ is non-negative, $k^* \leq \frac{2\partial_q V}{D}$. A standard method of dealing with non-Gaussian noise is to approximate ϕ with the first non-zero term in its Taylor expansion, which is of order 2 at least since ϕ is even. This approximation qualitatively shows the same behavior as Gaussian escape, but is at a higher value of $D_{eff} = D + \lambda\sigma^2(\rho)$, resulting in a lower action. The actual action will be smaller than this because of contributions from higher order terms in the expansion of ϕ. The path integral formalism allows the investigation of these contributions.

The interesting behaviour for the shot noise can be shown to happen in the $\lambda \to 0$ limit for fixed a[14]. Intuitively, for a given q, sending $\lambda \to 0$ means that k^* has to increase to balance the equation in (1.24). If k^* increases sufficiently, the higher order terms become relevant and the Gaussian approximation can break down.

ρ is classified into 3 types based on the nature of ϕ.

1. Type one noises have a ϕ that is finite and defined everywhere. For example, if $\rho(x) = \frac{1}{2}\delta(x-1) + \frac{1}{2}\delta(x+1)$, $\phi(x) = \cosh(x) - 1$
2. For type two noises, ϕ is defined only over a finite interval and has a singularity

at the boundaries. For example, an exponentially distributed $\rho(x) = \frac{1}{4}\exp(|x|)$ has $\phi(x) = \frac{x^2}{2(1-x^2)}$ for $x \in [-1, 1]$

3. For type three noises, ϕ is bounded and defined only over a finite interval, but its derivatives have a singularity at the boundaries.

Since everything remains finite for type-1 noises, the $\lambda \to 0$ limit is continuous, i.e. we only see Gaussian behavior. For type-2 noises, the singularities at ±1 essentially act as a cut-off to k^* going beyond $\pm\frac{1}{a}$. For small λ, if $\partial_q V < \frac{D}{2a}$, we see Gaussian behavior as (1.24) is satisfied by setting $k^* = \frac{2\partial_q V}{D}$ and since this is less than $\frac{1}{a}$, the contribution due to ϕ is zero. If $\partial_q V > \frac{D}{2a}$, ϕ needs to contribute to satisfy (1.24). For any small but finite λ, by getting k^* closer and closer to $\frac{1}{a}$, the RHS can be increased sufficiently to match $\partial_q V$. Thus the Lagrangian has the form $\min\left(\frac{\partial_q V}{2D}, \frac{1}{a}\right) \leq \mathcal{L}_{GWN}$. This shows that the $\lambda \to 0$ limit is discontinuous. From the stationarity condition for k^*,

$$\dot{q} = \psi'(k^*) - \partial_q V = \psi'(k^*) - \frac{\psi(k^*)}{k^*} \tag{1.25}$$

implies that $\dot{q} \to \infty$ as $k \to \frac{1}{a}$. Physically, this is manifested as the particle “jumping” over regions where $\partial_q V \geq \frac{D}{2a}$. This is only true in the limit though as for small but finite λ, k^* does not reach the cut-off.

For type-3 noises, (1.24) can not be satisfied for $\partial_q V$ sufficiently large, since ϕ is bounded. However this equation is predicated on the optimal speed being finite which is not the case.

$$\frac{\mathrm{d}}{\mathrm{d}\dot{q}}\left(\frac{\mathcal{L}}{\dot{q}}\right) = -\frac{\mathcal{L}}{\dot{q}^2} + \frac{1}{\dot{q}}\frac{\mathrm{d}\mathcal{L}}{\mathrm{d}\dot{q}} \tag{1.26}$$

$$= -\frac{1}{\dot{q}^2}\left[k^*(\dot{q} + \partial_q V) - \psi(k^*) - k^*\dot{q}\right] \tag{1.27}$$

$$= -\frac{1}{\dot{q}^2}\left[k^*\partial_q V - \psi(k^*)\right] \tag{1.28}$$

Since $k^* \in [-\frac{1}{a}, \frac{1}{a}]$, the RHS is always negative if $\partial_q V > \max_k \frac{\psi(k)}{k}$. If $\partial_q V > \frac{D}{2a}$, this can be ensured by making λ sufficiently small. Then, the optimal velocity is infinite. Unlike type-2 noises, the trajectory can have jumps even for finite λ, not just in the $\lambda = 0$ limit. As $\dot{q} \to \infty$, $\frac{\mathcal{L}}{\dot{q}} \to k^*$ and the maximization condition for k^* gives $k^* = \frac{1}{a}$. Thus the Lagrangian during the jump is the same for type-2 and type-3 noises. Since the trajectory is discontinuous, solving the Hamilton's equations is not equivalent to finding the stationary point of the action since it presumes smoothness of q and k.

Chapter 2

Methods

This chapter describes the methods used to find most probable escape trajectories. In Section 2.1, the details of two types of potentials used are given. In Section 2.2, the method used to solve Hamilton's equations is briefly described. Finally in Section 2.3, the path based optimization technique used for action minimization is discussed. This is done in greater detail because there was no pre-existing implementation suited to this problem.

2.1 Potentials used

We study the escape behavior in 2 types of potential. The first is a simple anisotropic Harmonic well.

$$V(x, y) = \frac{\lambda_x^2}{2}x^2 + \frac{\lambda_y^2}{2}y^2 \tag{2.1}$$

For the numerics, we will always set $\lambda_x = 0.1$ and $\lambda_y = 0.3$. We set the initial point at the bottom of the well (0,0). The particle is considered escaped if it reaches some final point (x_f, y_f). For simplicity, it is assumed that $x_f > 0$ and $y_f > 0$. The symmetry of the potential with respect to reflection about the x and y axes means that this is sufficient to describe all escape trajectories in the plane. The standard escape point will be (5.0,8.16). This corresponds to a well depth of 11.23. The harmonic potential is useful because it is simple enough for analytical solutions and a test for the numerics. The simplicity of the potential also means that features of the noise are in focus.

The next type of potential we use is a double well of the form

$$V(x, y) = g(y)\left[f_{\text{bar}}(x) - f_{\min}(x)\right] + f_{\min}(x) \tag{2.2}$$

where

$$g(y) = (y-1)^2(y+1)^2 \tag{2.3}$$

$$f_{\text{bar}}(x) = 1 + \frac{kx^2}{2} \tag{2.4}$$

$$f_{\text{min}}(x) = c\ln(\cosh(\lambda x)) \tag{2.5}$$

This has two stable fixed points at $(0, \pm 1)$ and a saddle at the origin. The starting point is at $(0, -1)$ and the escape point at $(0, 1)$. The parameters for the potential are $\lambda = 2.5, c = 0.12$ and $k = 0.1$. The reason for choosing this particular form of a double well is that there are two distinct types of escape strategies seen here; one where the escape path is similar to the passive case and one where the particle leverages its self propulsion to move around the barrier rather than over it. This potential is useful to study the preferance between the two types. In the present work, only Gaussian escape from the double well is considered.

2.2 Numerical solutions to Hamiltons equations

The Hamilton's equations are numerically solved using the BoundaryValueDiffEq.jl package that is part of the DifferentialEquations ecosystem[20]. This allows us to set $x(0), y(0), x(t_f), y(t_f)$ and $k_\theta(0) = k_\theta(t_f) = 0$ for some finite t_f. This package has many choices of methods for solving a boundary value problem. We use the MIRK4 solver, which is a collocation method. It uses a set of functions (like polynomials) that require a finite number of constant coefficients to be uniquely described. The boundary values and the differential equation at discretized points in $(0, t_f)$ give a system of non-linear equations for the coefficients. For an appropriate number and distribution of these discretized points, a unique and accurate solution can be obtained.

This method works well for Gaussian and type-1 angular noise. For type-2 noise, the use of continuous functions as a basis can mask jumps in θ in the $\lambda \to 0$ limit. For type-3 noise, the jump trajectories are not solutions of Hamilton's equations, so this is not useful.

A limitation of this method is that we only get finite time solutions. For the persistent limit when there is only GWN ($D_\theta \to 0$,$\lambda = 0$), it can be shown analytically that the finite time solutions converge to the analytical solution in a well-behaved manner as $t \to \infty$[15]. This seems true even for non-zero D_θ and λ where we do not have analytical results. Based on numerical results, the action decreases monotonically with increase in t_f and the trajectories converge.

2.3 The Geometric Minimum Action Method

2.3.1 Principles

The two major limitations of using the colocation method are that it gives only finite time solutions and can not handle potential landscapes that are more complex than the harmonic well. The dependence of action on total trajectory time suggests that minimum action trajectories take an infinite time to reach and leave fixed points. To find the most likely escape path, we are interested in

$$\min_{\mathbf{q},t_f} \max_{\mathbf{k}} S(\mathbf{q},\mathbf{k},t_f)\mathrm{d}t \tag{2.6}$$

Solving Hamilton's equations with the colocation method essentially amounts to performing the min-max in $\mathbf{q}$ and $\mathbf{k}$ for a fixed t_f. The Geometric Minimum Action Method(GMAM) performs all three optimization operations together by using a Gradient Descent-Ascent(GAD) algorithm for the min-max in $\mathbf{q}$ and $\mathbf{k}$ and doing a path based reparametrization. We use an implementation of the algorithm given in [21] with minor variations.

To rewrite the dependence on t_f, physical time is parametrized as $t(s)$ for $s \in [0,1]$ with $\frac{dt}{ds} = \frac{1}{\gamma}$. Thus, if $\gamma(s) = 0$ for some $s \in (0,1)$ it implies that the particle takes infinite time to reach and leave some point on the trajectory. It is necessary that $\gamma \geq 0$ for a proper parametrization. In terms of the new variable γ, The minimum action path satisfies

$$\min_{\mathbf{q}(t),\gamma} \max_{\mathbf{k}(t)} \int_0^1 \dot{\tilde{\mathbf{q}}} \cdot \tilde{\mathbf{k}} - \frac{1}{\gamma}\mathcal{H}(\tilde{\mathbf{q}},\tilde{\mathbf{k}})\mathrm{d}s \tag{2.7}$$

where $\tilde{\mathbf{q}}(s) = \mathbf{q}(t(s))$, $\tilde{\mathbf{k}}(s) = \mathbf{k}(t(s))$ and the derivatives are with respect to s. The tildes will be dropped for the remainder of this section because we are going to mostly with the reparametrized variables. If not, the difference will be highlighted by denoting the variables as $\mathbf{q}(t)$, $\mathbf{k}(t)$.

The additional variational degree of freedom introduced by γ is constrained by insisting that $||\frac{d\mathbf{q}}{ds}||$ be constant (but not fixed) throughout any given trajectory $\mathbf{q}(s)$. This constant is the total path length and the optimization over t_f is encoded in it.

γ is defined implicitly in terms of the path as follows: performing a point wise maximization in $\mathbf{k}$ first,

$$\gamma\dot{\mathbf{q}} = \nabla_{\mathbf{k}}\mathcal{H}(\mathbf{q},\mathbf{k}) \tag{2.8}$$

Inverting this equation allows us to write $\mathbf{k}$ in terms of $\mathbf{q}, \dot{\mathbf{q}}$ and γ as $\mathbf{k} = \Phi(\mathbf{q},\dot{\mathbf{q}},\gamma)$. This is possible because $\mathcal{H}$ is convex in $\mathbf{k}$. Then, we perform the minimization in γ

keeping in mind the dependence of $\mathbf{k}$ on γ:

$$\dot{\mathbf{q}} \cdot \partial_\gamma \Phi + \frac{1}{\gamma^2}\mathcal{H}(\mathbf{q}, \mathbf{k}) - \frac{1}{\gamma}\nabla_{\mathbf{k}}\mathcal{H} \cdot \partial_\gamma \Phi = 0 \tag{2.9}$$

Note that plugging (2.3.1) for $\dot{\mathbf{q}}$ gives $\mathcal{H}(\mathbf{q}, \mathbf{k}) = 0$. This is true if the optimizations in $\mathbf{k}$ and γ are done. Thus, a check for convergence is whether $\mathcal{H} = 0$ throughout the trajectory. To proceed, we try to invert Φ to rewrite γ as a function of $\mathbf{q}, \dot{\mathbf{q}}$. It is in general not true that this inversion is possible, but at convergence, the Hamilton's equation for $\mathbf{k}$ can be inverted as $\mathcal{H}$ is convex in $\mathbf{k}$.

$$\gamma \dot{\mathbf{q}} = \nabla_{\mathbf{k}}\mathcal{H} \tag{2.10}$$

$$\dot{\mathbf{q}} = (\nabla^2_{\mathbf{k}}\mathcal{H})\partial_\gamma \Phi \tag{2.11}$$

$$\partial_\gamma \Phi = C\dot{\mathbf{q}} \tag{2.12}$$

where $C = (\nabla^2_{\mathbf{k}}\mathcal{H})^{-1}$. Plugging this back into (2.9) and solving the resulting quadratic equation for γ, we get

$$\gamma = \frac{\nabla_{\mathbf{k}}\mathcal{H} \cdot (C\dot{\mathbf{q}}) + \sqrt{[\nabla_{\mathbf{k}}\mathcal{H} \cdot (C\dot{\mathbf{q}})]^2 - 4\mathcal{H}\dot{\mathbf{q}} \cdot C\dot{\mathbf{q}}}}{2\dot{\mathbf{q}} \cdot C\dot{\mathbf{q}}} \tag{2.13}$$

Since it is not necessarily true that this candidate for γ is non-negative before convergence, we make some modifications to ensure that it is.

$$\gamma = \frac{|\nabla_{\mathbf{k}}\mathcal{H} \cdot (C\dot{\mathbf{q}})| + \sqrt{[\nabla_{\mathbf{k}}\mathcal{H} \cdot (C\dot{\mathbf{q}})]^2 - 4\mathcal{H}\dot{\mathbf{q}} \cdot C\dot{\mathbf{q}}}}{2\dot{\mathbf{q}} \cdot C\dot{\mathbf{q}}} \tag{2.14}$$

For our problem, C is just

$$\begin{bmatrix} \frac{1}{D} & 0 & 0 \\ 0 & \frac{1}{D} & 0 \\ 0 & 0 & \frac{1}{D_\theta} \end{bmatrix} \tag{2.15}$$

Since we have γ as a function of $\mathbf{q}$ and $\mathbf{k}$ at each optimization time step, we can use a two timescale gradient descent-ascent approach to optimize the action.

$$\partial_\tau \mathbf{q} = -\alpha \frac{\delta S}{\delta \mathbf{q}(t)} = \alpha\gamma\dot{\mathbf{k}} + \alpha\nabla_{\mathbf{q}}\mathcal{H} \tag{2.16}$$

$$\alpha\partial_\tau \mathbf{k} = \frac{\delta S}{\delta \mathbf{k}(t)} = \gamma\dot{\mathbf{q}} - \nabla_{\mathbf{k}}\mathcal{H} \tag{2.17}$$

Here, τ is the optimization time and α is the ascent-descent timescale. $\alpha \to 0$ correponds to calculating the Legendre transform.

2.3.2 Algorithm

For the numerics, it is useful to redefine the $\mathbf{q}$ and $\mathbf{k}$ as $\mathbf{u} = \mathbf{q} + \alpha\mathbf{k}$ and $\mathbf{v} = \mathbf{q} - \alpha\mathbf{k}$. In terms of these variables, the gradient ascent-descent equations are of the form

$$\partial_\tau \mathbf{u} = \gamma\dot{\mathbf{u}} + \mathbf{f}(\mathbf{u}, \mathbf{v}) \tag{2.18}$$

$$\partial_\tau \mathbf{v} = -\gamma\dot{\mathbf{v}} + \mathbf{g}(\mathbf{u}, \mathbf{v}) \tag{2.19}$$

Where $\mathbf{f}$ and $\mathbf{g}$ are given by

$$\mathbf{f}(\mathbf{u}, \mathbf{v}) = \alpha\nabla_{\mathbf{q}}\mathcal{H} - \nabla_{\mathbf{k}}\mathcal{H} \tag{2.20}$$

$$\mathbf{g}(\mathbf{u}, \mathbf{v}) = \alpha\nabla_{\mathbf{q}}\mathcal{H} + \nabla_{\mathbf{k}}\mathcal{H} \tag{2.21}$$

The conversion from $\mathbf{u}, \mathbf{v} \to \mathbf{q}, \mathbf{k}$ has been made implicitly. The boundary conditions for the components of $\mathbf{u}, \mathbf{v}$ are $\frac{u_b + v_b}{2} = q_b$ or $\frac{u_b - v_b}{2\alpha} = k_b$ depending on whether the position q_b or momentum k_b is fixed at the boundary.

A straightforward implementation of algorithm 4 from [21] i.e. gradient descent-ascent with a path length reparametrization is used. The major difference is that instead of fixing θ at the ends, k_θ needs to be zero. This is easily done by modifying the update equations for both end points. Equations (2.22)-(2.29) are update equations for $\mathbf{u}$ and $\mathbf{v}$. For the discretized update equations, upper indices denote optimization time step, lower indices denote points along the path. The unit interval is discretized into n points and the parametrized curve $[\mathbf{q}(s), \mathbf{k}(s)]$ is discretized accordingly. Each point is evolved in the optimization time τ. First, $\mathbf{u}$ is updated from $s = 1 \to 0$ and then $\mathbf{v}$ from $s = 0 \to 1$ as follows:

First convert $\mathbf{q}^\tau, \mathbf{k}^\tau$ to $\mathbf{u}^\tau, \mathbf{v}^\tau$ as $\mathbf{u}^\tau = \mathbf{q}^\tau + \alpha\mathbf{k}^\tau$, $\mathbf{v}^\tau = \mathbf{q}^\tau - \alpha\mathbf{k}^\tau$.

Then, $\mathbf{u}$ is updated.

Depending on the boundary conditions, point n is updated as

$$\mathbf{u}_n^{\tau+1} = -\mathbf{v}_n^\tau + 2\mathbf{q}_\mathbf{f} \tag{2.22}$$

Or if there are mixed boundary conditions, e.g. if (x, y) is fixed as $\mathbf{q}_f$ and $k_\theta(1) = 0$, the x, y components $\mathbf{u}_n^{\tau+1}(x, y)$ and θ component $\mathbf{u}_n^{\tau+1}(\theta)$ are updated as

$$\mathbf{u}_n^{\tau+1}(x, y) = -\mathbf{v}_n^\tau(x, y) + 2\mathbf{q}_\mathbf{f}(x, y) \text{ and } \mathbf{u}_n^{\tau+1}(\theta) = \mathbf{v}_n^\tau(\theta) \tag{2.23}$$

A first order discretization of $\dot{\mathbf{u}}$ is used for point $n-1$:

$$\mathbf{u}_{n-1}^{\tau+1} = \frac{1}{1 + r\gamma_{n-1}^{\tau}} \left(r\gamma_{n-1}^{\tau}\mathbf{u}_{n}^{\tau+1} + \Delta\tau\mathbf{f}(\mathbf{q}_{n-1}^{\tau}, \mathbf{k}_{n-1}^{\tau}) + \mathbf{u}_{n-1}^{\tau} \right) \tag{2.24}$$

A second order discretization scheme is used for all other points:

$$\mathbf{u}_{i}^{\tau+1} = \frac{1}{1 + 1.5r\gamma_{i}^{\tau}} \left(2r\gamma_{i}^{\tau}\mathbf{u}_{i+1}^{\tau+1} - 0.5r\gamma_{i}^{\tau}\mathbf{u}_{i+2}^{\tau+1} + \Delta\tau\mathbf{f}(\mathbf{q}_{i}^{\tau}, \mathbf{k}_{i}^{\tau}) + \mathbf{u}_{i}^{\tau} \right) \tag{2.25}$$

Where $r = \frac{\Delta\tau}{\Delta s}$. After updating $\mathbf{u}$, recalculate $\mathbf{q}, \mathbf{k}$ and reparametrize them as $\hat{\mathbf{q}}, \hat{\mathbf{k}}$ so that $||\dot{\hat{\mathbf{q}}}|| =$ constant. Then find the $\tilde{\gamma}$ corresponding to $\hat{\mathbf{q}}, \hat{\mathbf{k}}$. These intermediate values are used for updating $\mathbf{v}$.

The update equations are exactly the same, but run the other way from $1 \to n$ and the Hamiltonian term is $\mathbf{g}$ instead of $\mathbf{f}$.

Depending on boundary conditions, point 1 is updated as:

$$\mathbf{v}_{1}^{\tau+1} = -\mathbf{u}_{1}^{\tau+1} + 2\mathbf{q}_{i} \tag{2.26}$$

$$\mathbf{v}_{1}^{\tau+1}(x, y) = -\mathbf{u}_{1}^{\tau+1}(x, y) + 2\mathbf{q}_{i}(x, y) \text{ and } \mathbf{v}_{1}^{\tau+1}(\theta) = \mathbf{u}_{1}^{\tau+1}(\theta) \tag{2.27}$$

First order for point 2:

$$\mathbf{v}_{2}^{\tau+1} = \frac{1}{1 + r\tilde{\gamma}_{2}^{\tau}} \left(r\tilde{\gamma}_{2}^{\tau}\mathbf{v}_{1}^{\tau+1} + \Delta\tau\mathbf{g}(\hat{\mathbf{q}}_{2}^{\tau}, \hat{\mathbf{k}}_{2}^{\tau}) + \mathbf{v}_{2}^{\tau} \right) \tag{2.28}$$

Second order for all other points:

$$\mathbf{v}_{i}^{\tau+1} = \frac{1}{1 + 1.5r\tilde{\gamma}_{i}^{\tau}} \left(2r\tilde{\gamma}_{i}^{\tau}\mathbf{v}_{i-1}^{\tau+1} - 0.5r\tilde{\gamma}_{i}^{\tau}\mathbf{v}_{i-2}^{\tau+1} + \Delta\tau\mathbf{g}(\hat{\mathbf{q}}_{i}^{\tau}, \hat{\mathbf{k}}_{i}^{\tau}) + \mathbf{v}_{i}^{\tau} \right) \tag{2.29}$$

From this, obtain $\mathbf{q}^{\tau+1}, \mathbf{k}^{\tau+1}$,reparametrize and calculate $\gamma^{\tau+1}$.

The reparametrization is done similar to the string method [22]: the parameter value s_i corresponding to point i is calculated as $\sum_{j=2}^{i} |q_j - q_{j-1}|$ for $i > 0$ and 0 for $i = 0$. It is normalized by s_n so that the parameter values lie on the unit interval. Using the Dierckx.jl package, we calculate a parametric spline interpolation through the phase space path $(\mathbf{q}^{\tau+1}, \mathbf{k}^{\tau+1})$ The path $\mathbf{q}(s), \mathbf{k}(s)$ for the next time step is now obtained. This is then discretized uniformly and we get $\gamma^{\tau+1}$ to repeat the procedure. We use 2nd or 3rd order spline interpolation depending on the speed needed. This interpolation procedure works quite well.

Other aspects of the algorithm like stability, convergence and dependence on initial conditions are discussed in the context of the present problem in the next section.

Chapter 3

Results and discussion

In Section 3.1 we describe Gaussian escape from the harmonic well, describing the minimum action path analytically in the persistent limit[10] and verify them using the collocation method. We see that finite time collocation solutions match those obtained in [15]. We compare the collocation solutions with the GMAM solutions in Section 3.2. This is done separately to discuss the numerical details of the implementation used without interrupting the physics. In Section 3.3 we discuss numerical results from the collocation method for type-1 shot noise and compare them to the features of 1-d escape in the presence of PSN found in [14]. In Section 3.4, we derive analytical results for type-2 trajectories in the persistent limit and generate examples of escape trajectories with jumps in θ. We also discuss how the collocation performs in the approach to the persistent limit. Finally, in Section 3.5 we discuss the GMAM results for a double well potential, the two distinct types of escape trajectories seen and their dependence on the persistence time and self propulsion speed. Numerical details in the context of the double well are then discussed. The work in this last section was done in close collaboration with Dr. Rafael Díaz.

3.1 Gaussian escape from an elliptic potential

Before looking at the effects of the PSN, we switch it off by setting $\lambda = 0$ to study how the particle behaves under pure GWN. In this case, the Legendre transform can be performed explicitly by a pointwise maximization.

$$\frac{\partial \mathcal{L}}{\partial k_x} = 0 \implies k_x = \frac{2}{D}(\dot{x} - v\cos\theta + \partial_x V) \tag{3.1}$$

$$\frac{\partial \mathcal{L}}{\partial k_y} = 0 \implies k_y = \frac{2}{D}(\dot{y} - v\sin\theta + \partial_y V) \tag{3.2}$$

$$\frac{\partial \mathcal{L}}{\partial k_\theta} = 0 \implies k_\theta = \frac{\dot{\theta}}{D_\theta} \tag{3.3}$$

With this, the Lagrangian can be written down explicitly. It has an Onsager-Machlup form as shown below[23].

$$\mathcal{L} = \frac{1}{2D}[(\dot{x} - v\cos\theta + \partial_x V)^2 + (\dot{y} - v\sin\theta + \partial_x V)^2] + \frac{\dot{\theta}^2}{2D_\theta} \tag{3.4}$$

Thus, we can also get the Euler Lagrange equations corresponding to the Hamilton's equations of the MSR action. For the numerics, we will stick to solving the Hamilton's equations as it will serve as useful check to verify the results in [15] and [10]. However, some insights can still be gained from the Lagrangian that will be applicable even in the Hamiltonian setup for $\lambda \neq 0$.

It can be noticed from (3.4) that as long as $-v\cos\theta + \partial_x V < 0$, one can have an $\dot{x} > 0$ with $(\dot{x} - v\cos\theta + \partial_x V) = 0$ by setting $\dot{x} = v\cos\theta - \partial_x V$. By a similar operation in y and setting θ constant, it is possible to move with zero Lagrangian. This motion is essentially gradient descent in an effective potential $\dot{\mathbf{r}} = -\nabla V^{\theta}_{eff}$ where

$$V^{\theta}_{eff}(x, y) = V(x, y) - xv\cos\theta - yv\sin\theta \tag{3.5}$$

For small enough v or a far enough final point, this is no longer possible beyond a point because ∇V^{θ}_{eff} increases with $||\mathbf{r}||$ and is positive for large $\mathbf{r}$. This means a positive $\dot{\mathbf{r}}$ can no longer be sustained with zero Lagrangian.

For the harmonic potential, these gradient descent trajectories are given below:

$$x(t) = \frac{v\cos\theta}{\lambda_x}(1 - e^{-\lambda_x t}) \tag{3.6}$$

$$y(t) = \frac{v\sin\theta}{\lambda_y}(1 - e^{-\lambda_y t}) \tag{3.7}$$

As $t \to \infty$, $(x, y) \to \left(\frac{v\cos\theta}{\lambda_x}, \frac{v\sin\theta}{\lambda_y}\right)$. For varying $\theta \in [0, 2\pi]$, this contour of fixed points describe an ellipse with the equation

$$\lambda_x^2 x^2 + \lambda_y^2 y^2 = 1 \tag{3.8}$$

We will call this ellipse C_1 (in case of more complicated potential landscapes, there can be multiple such regions). Since the interior of this ellipse is covered by the set of all gradient descent trajectories of different θ (that are fixed in time), any point lying inside it can be reached with zero action. Since the Lagrangian is non-negative, this means that gradient descent trajectories are always preferred inside C_1.

Note that in the Hamiltonian formalism, this means that $k_x = k_y = k_\theta = 0$. This is consistent with the ks representing the effect of noise on the system. Since the particle essentially travels downhill by properly orienting the self propulsion force, this means that the particle can reach points inside C_1 even in the absence of noise, thus having no action cost.

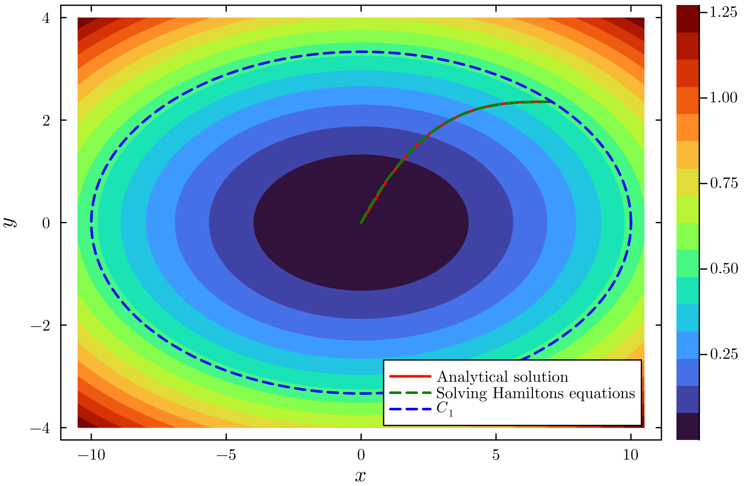

Figure 3.1: The colour bar shows $V(x, y)$. The final point for the trajectories corresponds to the one on C_1 with $\theta = \frac{\pi}{4}$. The red solid line is the analytical solution given in (3.6) and (3.7). The green dashed line is obtained by solving the Hamilton's equations numerically. The blue dashed line is the C_1 contour.

Trajectories like the one shown above (that pass through a fixed point of the noiseless dynamics) take an infinite time to reach the final point. For final points on C_1, it is obvious that the minimal action trajectory takes an infinite total time. However, numerical solutions of Hamilton's equations can be obtained only when the final point is reached in a finite total time. Thus, the action obtained from such methods will always be slightly larger than the actual value.

It can also be seen that the particle can move along C_1 quasi statically with zero action cost. This is done by varying θ, x, y slowly so that the x, y, θ always remains on C_1. For example, the $\dot{x}$ component of the cost of changing θ from $\theta_i = 0$ to $\theta_f = c\Delta$ with constant speed c is calculated below.

$$x = \frac{v\cos\theta}{\lambda_x} \tag{3.9}$$

$$\dot{x} = \frac{-cv\sin\theta}{\lambda_x} \tag{3.10}$$

$$S = \frac{1}{2D}\int_0^{\Delta} dt \left(\frac{-cv\sin(ct)}{\lambda_x}\right)^2 \tag{3.11}$$

$$= \frac{c^2v^2}{4D\lambda_x^2}\left(\Delta - \frac{\sin(2c\Delta)}{2c}\right) \tag{3.12}$$

As $c \to 0$ and $\Delta \to \infty$ with $c\Delta = \theta_f$, $S \to 0$. A similar calculation for the $\dot{y}$ term can also be done. The cost associated with the $\dot{\theta}$ term is just $\frac{c^2\Delta}{2D_\theta}$ which also goes to zero. Thus, there is a degeneracy in paths to points on C_1: the particle can fix and $\theta(0)$ and perform gradient descent to C_1 before quasi-statically diffusing to the correct final point. However, this is only really true when the total time for the trajectory is left unbounded. For finite time trajectories, the minimum action path is unique.

For final points outside C_1, there are no zero action trajectories and it is in general not possible to obtain an analytical solution. Since $\nabla V_{eff}^{\theta} > 0$ for any θ, as long as $\dot{\mathbf{r}} > 0$ somewhere along the trajectory, there is a cost.

3.1.1 Persistent limit

The high persistent time limit (just called the persistent limit for convenience) is when the timescales on which θ changes is much larger than timescales on which x and y change. This is imposed by taking the limit $D_\theta \to 0$ and $\lambda \to 0$. In this section where we are interested in Gaussian escape, λ is set to be exactly 0. In the persistent limit, the problem is still analytically tractable as θ remains constant. The Lagrangian can be rewritten as

$$\mathcal{L} = \frac{1}{2D}\left(||\dot{\mathbf{r}} - \nabla V_{eff}^{\theta}||^2 + 4\dot{\mathbf{r}}\cdot\nabla V_{eff}^{\theta}\right) + \frac{\dot{\theta}^2}{D_\theta} \tag{3.13}$$

Since D_θ is small, a non-zero $\dot{\theta}$ at any point in the trajectory will cause the Lagrangian to blow up. Thus θ always constant. For a constant θ, the second term in the brackets of (3.13) is path independent:

$$\int_{t_i}^{t_f} dt(\dot{\mathbf{r}}\cdot\nabla V_{eff}^{\theta}) = V_{eff}^{\theta}(\mathbf{r}(t_f)) - V_{eff}^{\theta}(\mathbf{r}(t_i)) \tag{3.14}$$

Thus, the first term is the one that needs to be minimized. This is done by setting $\dot{\mathbf{r}} = \nabla V_{eff}^{\theta}$. Since ∇V_{eff}^{θ} is positive outside C_1, this implies a positive $\dot{\mathbf{r}}$ as required. So, outside C_1 it is optimal to have trajectories that perform gradient ascent. The gradient ascent trajectories from C_1 to the final point are just time reversed versions of gradient descent trajectories from the final point to C_1 which are given in equations (3.15) and (3.16). For a final point (x_f, y_f), the time reversed gradient ascent trajectories are

$$x(t) = x_f e^{-\lambda_x t} + \frac{v\cos\theta}{\lambda_x}\left(1 - e^{-\lambda_x t}\right) \tag{3.15}$$

$$y(t) = y_f e^{-\lambda_y t} + \frac{v\sin\theta}{\lambda_y}\left(1 - e^{-\lambda_y t}\right) \tag{3.16}$$

where $t \in [0, \infty)$.

For $D_\theta \to 0$ and an escape point outside C_1, the escape path consists of a gradient descent to C_1 and a gradient ascent from C_1 to the final point with a constant θ.

For such a trajectory, the only non-zero action contribution is from the term in (3.14). Thus the action is just $\frac{2}{D}\Delta V_{eff}^{\theta}$. This makes sense as since θ is constant, this is essentially Gaussian escape in V_{eff}^{θ}. Since θ is free at the boundaries, the optimal escape path will be the gradient descent+ascent path with a

$$\theta^* = \arg\min_{\theta} V_{eff}^{\theta}(x_f, y_f) - V_{eff}^{\theta}\left(\frac{v\cos\theta}{\lambda_x}, \frac{v\sin\theta}{\lambda_y}\right) \tag{3.17}$$

For convenience, we will denote $\left(\frac{v\cos\theta}{\lambda_x}, \frac{v\sin\theta}{\lambda_y}\right)$ as $C_1(\theta)$. As in the case for points within C_1, there is a degeneracy in paths here too. The particle can perform gradient descent with any θ to C_1 and then diffuse quasi-statically to $C_1(\theta^*)$ and then perform gradient ascent from there. Thus, only the gradient ascent portion of the escape path is unique.

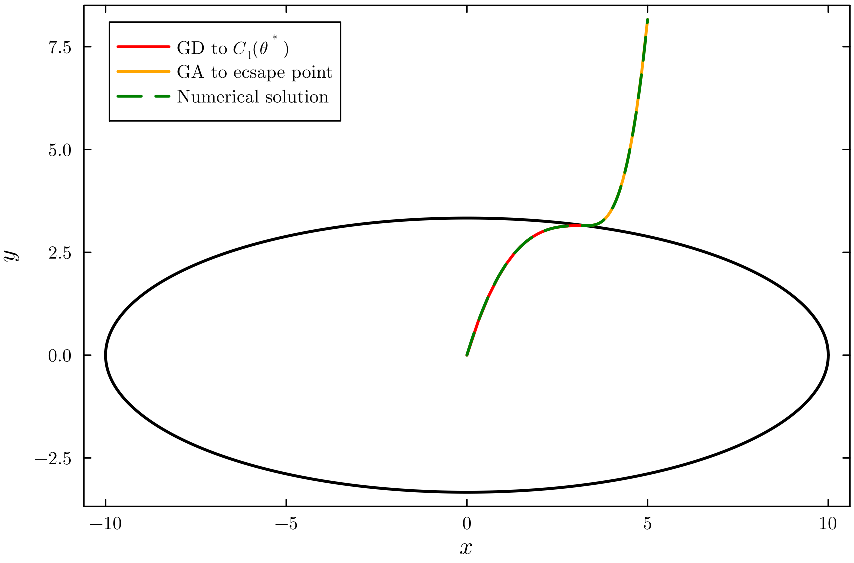

(a) Comparison of trajectories

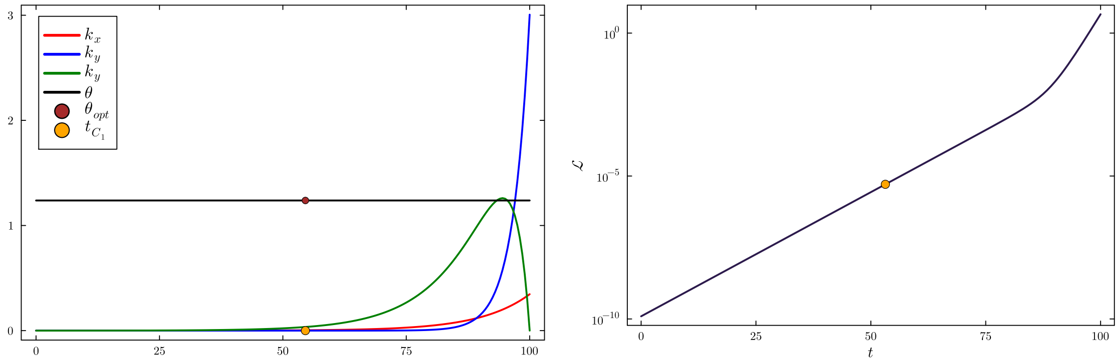

(b) The momenta and θ vs t

(c) The Lagrangian vs t

Figure 3.2: Comparison of analytical and numerical solutions. In (3.2b), t_{C1} is the time at which $(\lambda_x x)^2 + (\lambda_y y)^2 = 1$

In the graphs above, θ^* is calculated by optimizing the effective potential difference between the initial and final points. The solid lines in (3.2a) are analytical solutions for GD/GA trajectories with $\theta = \theta^*$.

It can be seen in (3.2b) that the numerical solution maintains constant $\theta = \theta^*$ as expected. It is seen that the ks are zero (or at least extremely small) during the gradient descent phase. Since the trajectory is fixed to have a finite time 100, they are not exactly zero at C_1. The trajectory still takes a majority of the total time to reach C_1 and a majority of the remaining time to move a very small distance out of C_1. The portion of the trajectory where the particle actually climbs from C_1 to the final point is seen as the region of (3.2c) with different slope. This is in line with barrier corssing having an exponential action cost.

The action for the numerical solution is 7.8291. The expected value of $\frac{2}{D}\Delta V_{eff}^{\theta^*}$ is 7.8290. As expected, the finite time trajectory has a slightly larger action.

3.1.2 Escape with $D_\theta > 0$

For non-zero D_θ, we have no analytical solution and hence need to solely use numerical methods. However, the persistent limit can still offer intuition.

One expects the action to monotonically decrease with D_θ From the Lagrangian (3.4), since the action associated with any given $\dot{\theta}(t)$ is decreased due to the larger value of D_θ in the denominator. Physically, it is easier for the particle to re-orient itself in response to the local potential landscape.

Even in the case of finite D_θ, we see a gradient descent with zero Lagrangian to C_1 and the most probable escape path can be found by just optimizing over initial points from C_1 with fixed initial θ.

$$S_{\min}(\mathbf{r_i}, \mathbf{r_f}) = \min_{\theta} S_{\min}(C_1(\theta), \mathbf{r_f}) \tag{3.18}$$

Unlike the persistent limit, there is no analytical form for $S_{\min}(C_1(\theta), \mathbf{r_f})$ so a direct numerical optimization of some objective function of θ is not possible.

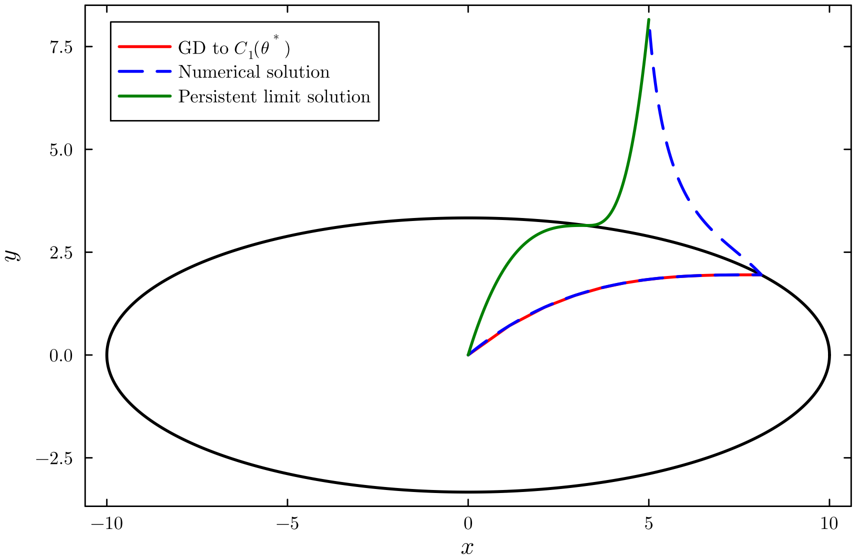

(a) Comparison of trajectories

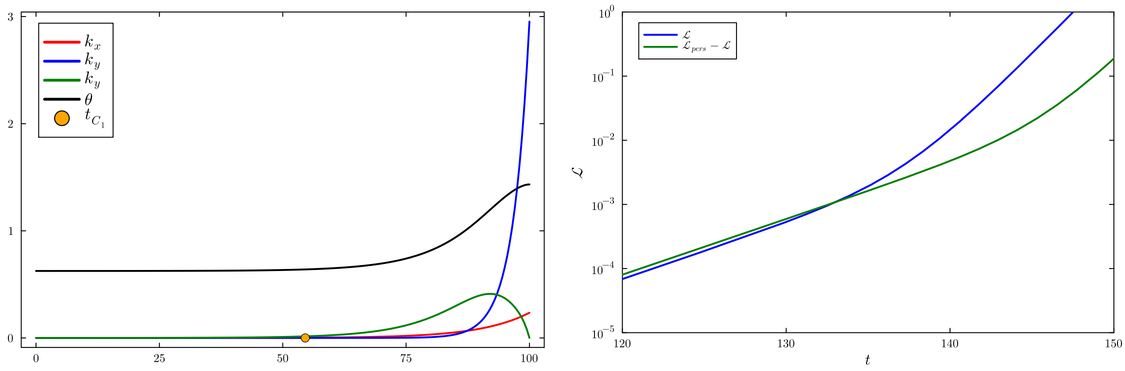

(b) The momenta and θ vs t

(c) Comparison of Lagrangians

Figure 3.3: Comparison of numerical solutions for $D_\theta = 0$ and $D_\theta = 0.1$.

The numerical solution for $D_\theta = 0.1$ shows the features mentioned above. It can also be seen that the trajectory is no longer time reversal symmetric. Interestingly, the gradient descent is to a point on C_1 that is closer to the x axis than to the final point. The post C_1 portion of the trajectory is also marked by a change in curvature. This behavior can be intuitively explained as follows: Our choice of λ_x and λ_y (0.1 vs 0.3) means that the well is steeper in the y-ward direction. Thus, it is better to keep the self propulsion direction closer to $\pi/2$ than to 0 to reduce the y-ward gradient more than the x-ward gradient. This is also reflected in the fact that $\theta^* > \frac{\pi}{4}$ in the persistent limit. It is therefore advantageous to "overshoot" x_f and leverage the negative x-ward potential gradient for a push towards x_f and focus the self propulsion on climbing the y barrier by pointing it close to $\frac{\pi}{2}$ as seen in Fig (3.3b). However, to leave C_1 close to the x axis, one needs to maintain $\theta = 0$. On leaving C_1, θ needs to increase to $\frac{\pi}{2}$. As seen in Fig. 3.3b, this portion of the trajectory happens in a very short time (it is called the instanton). Thus this required change in θ will have a fairly large action cost necessitating a large D_θ to offset it. This reduced action due to following a more eficient path is reflected in Fig. 3.3c, where the persistent limit solution always has a higher Lagrangian than the trajectory with $D_\theta = 0.1$.

This is a fairly crude argument though. As evidenced by the fact that $k_x > 0$ towards the end of the trajectory, one can not rely solely on the $-x$-ward potential gradient. Presumably, this gradient is too steep and takes the particle beyond x_f by the time y increases to y_f necessitating positive x-ward noise to slow the motion.

This trajectory has a total action of 7.5204, a significantly smaller value than in the persistent limit.

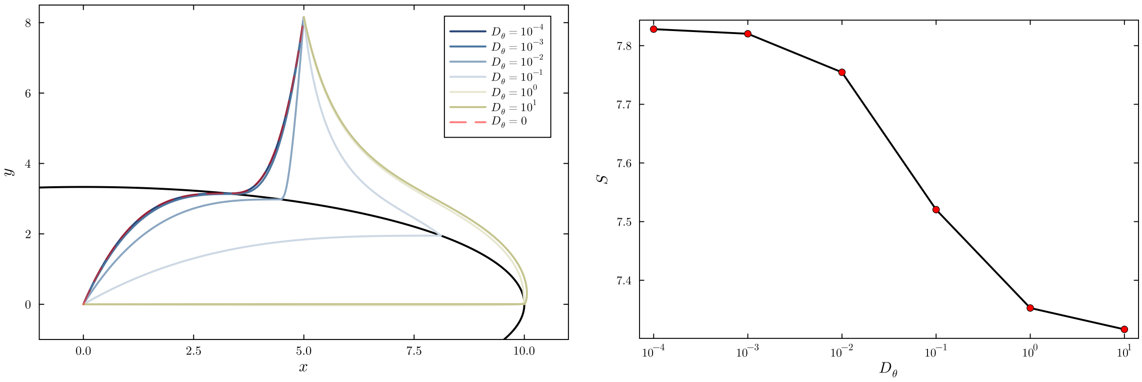

(a) Comparison of trajectories

(b) Action vs D_θ

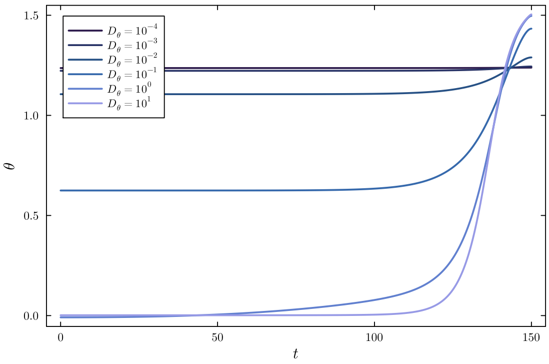

(c) θ vs t

Figure 3.4: Comparison of numerical solutions for different D_θ

As seen in Fig. 3.4, there is a continuous variation in paths between the persistent limit solution and a path leaving C_1 on the x axis as D_θ is increased. The corresponding actions also reduce smoothly. The increasingly sharp jump in θ to a value close to $\frac{\pi}{2}$ can be seen in Fig. (3.4c).

Fig. 3.5 shows that the full trajectory can be obtained by optimizing over different starting points on C_1 by finding the point that minimizes the cost of the instantonic climb. The full trajectories from (0.0,0.0) to the final point are first obtained for different D_θ. Then, the $C_1(\theta^*)$ at which it begins the instantonic portion is found. For each value of D_θ, action minimizing trajectories from $C_1(\theta^* + \delta\theta)$ to the final point are found for different $\delta\theta$s. For these trajectories, $\theta(0)$ is fixed instead of $k_\theta(0)$ ensuring that they do not have any gradient descent portions.

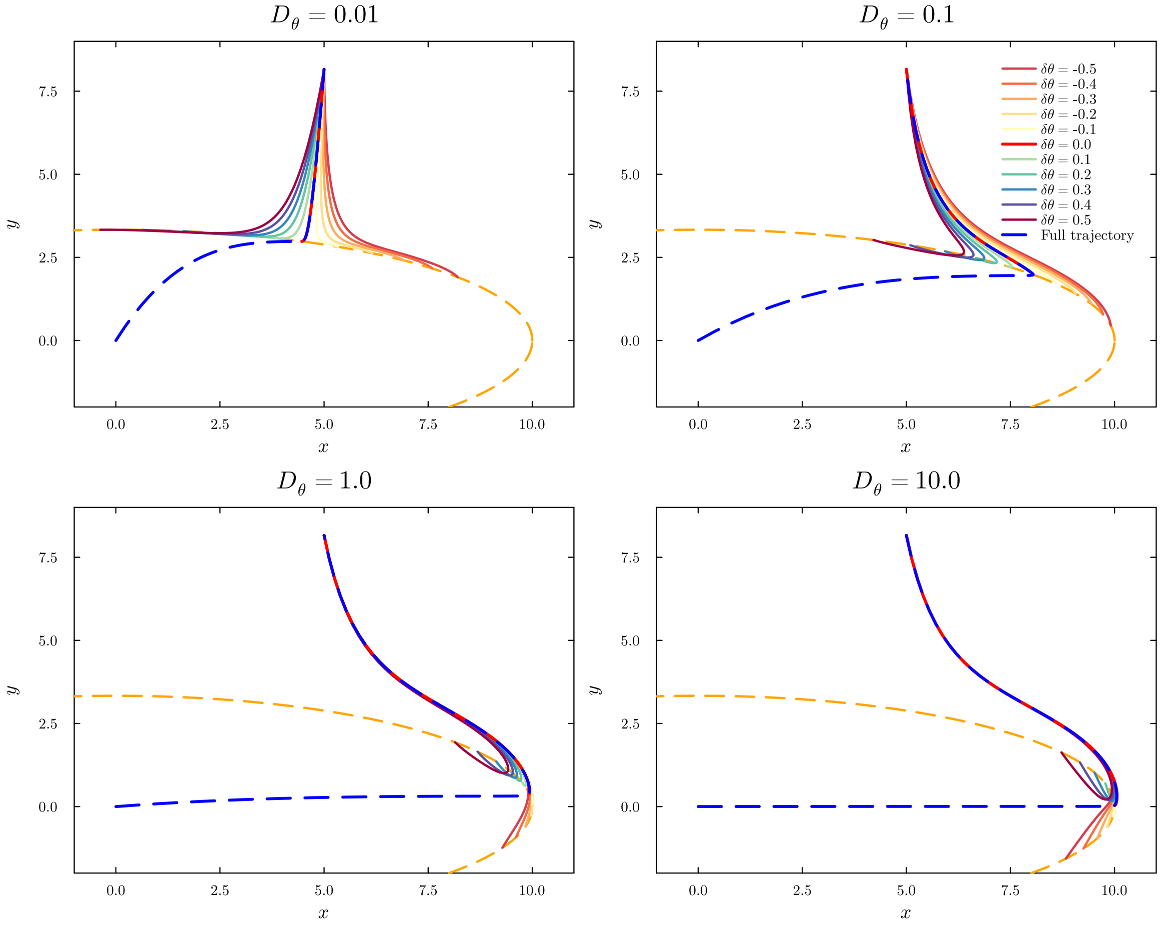

Figure 3.5: Perturbed trajectories for different values of $\delta\theta$ and D_θ

The previously mentioned degeneracy in leaving points on C_1 due to the possibility of quasi-static diffusion on C_1 is not seen in Fig. 3.5 because of the finite time condition on the trajectories. Although not shown, k_x, k_y and k_θ are zero in the beginning of the trajectories, suggesting that even for fixed, non-optimal leaving point on C_1, the gradient descent + instantonic path is most likely.

The actions for these non-optimal trajectories are shown in Fig. 3.6

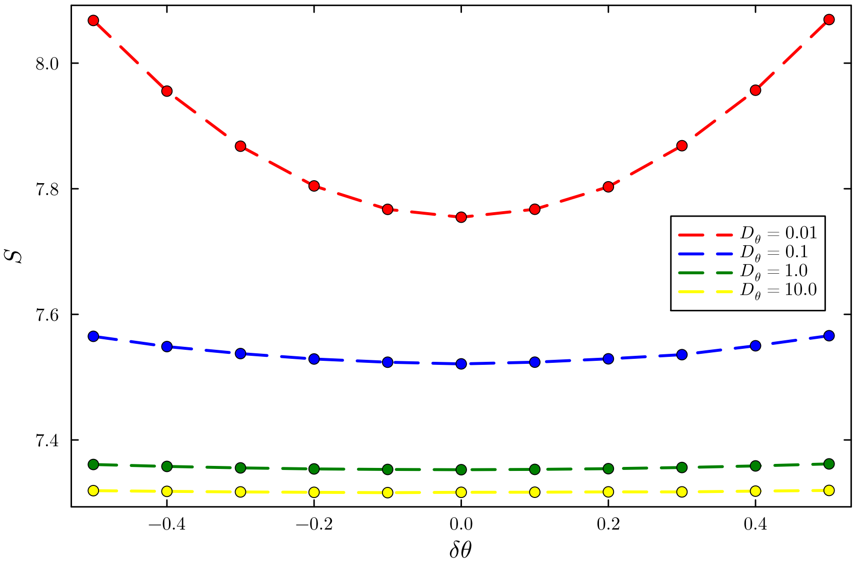

Figure 3.6: Action vs $\delta\theta$ for different D_θ

Fig. 3.6 shows the dependence of the action on the leaving point on C_1. For increasing D_θ, this graph is very flat. This shows that the particle can re-orient its self propulsion fast enough that the leaving point on C_1 has a smaller effect on the total action. Thus the strategy of optimizing over trajectories from C_1 is harder for large D_θ.

3.2 GMAM solutions - Harmonic potential

In this section, we mostly discuss the numerical aspects of the GMAM implementation and compare the solutions to those obtained by the collocation method. The GMAM is in general quite sensitive to parameter choices and initial conditions. This is partly because we use the Hamilton formalism. There are versions of the GMAM that are designed to minimize the action from a Lagrangian that perform better in the case of Gaussian escape[24][25]. However, for type-3 noise where we do not have the Lagrangian and solving the Hamilton's equations is a no-go, this might be helpful. In the present work where we have only considered Gaussian noise, the harmonic well functions as a good test for the GMAM since we have analytical results and trajectories from the collocation method.

As seen in Fig. 3.7, the GMAM works quite well in the persistent limit, much better than for larger values for D_θ. This is probably because the solution does not move to a point on C_1 close to the x axis and then curve back.

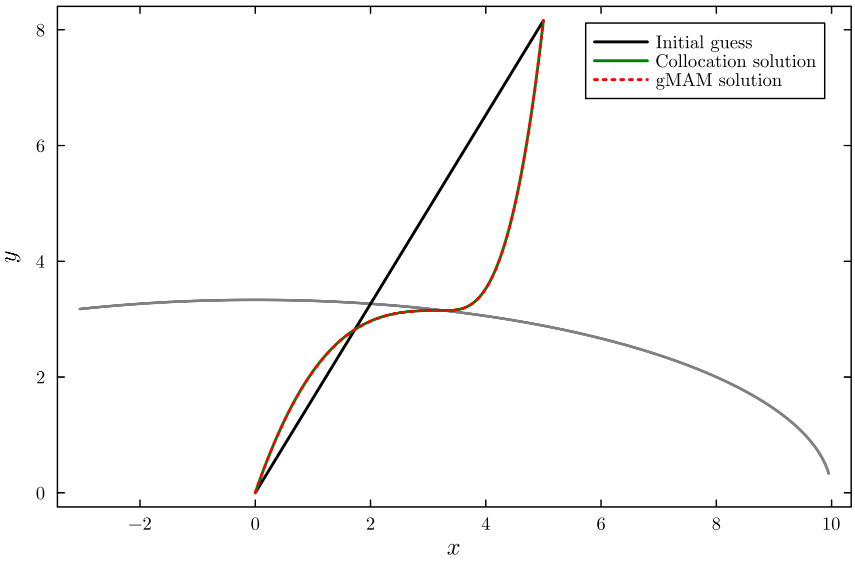

(a) x and y in the persistent limit.

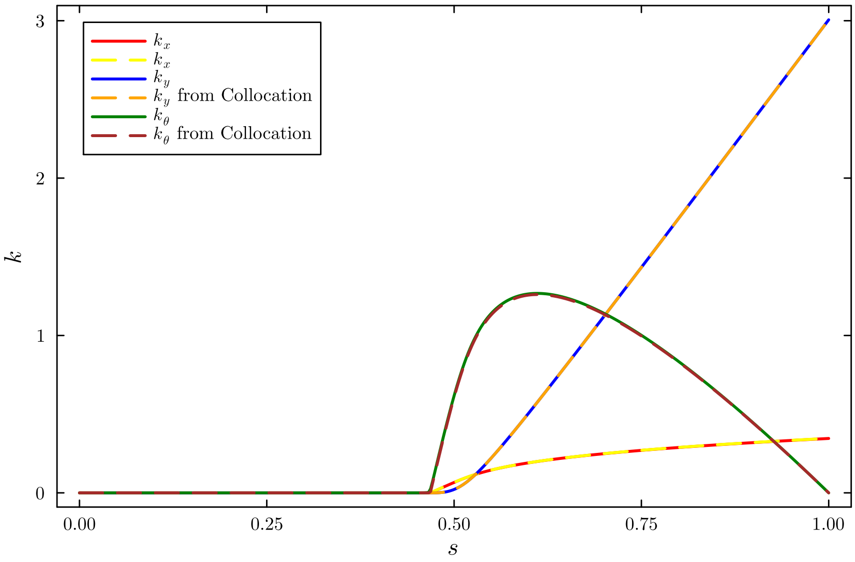

(b) k_x, k_y and k_θ for the GMAM and reparametrized colocation trajectory

Figure 3.7: Comparison of the GMAM and collocation solutions in the persistent limit

The final action for the solution in Fig. 3.7 is 7.84959. The colocation trajectory has an action of 7.82906. This is probably because the GMAM action is calculated from a discretized trajectory. On reparametrizing and discretizing the colocation trajectory, it has an action of 7.84960.

It seems that smaller values of α are better in general. If α is too large, the GAD does not converge. This is expected as the proof for convergence in [21] only works for small α. Intuitively, a smaller α means that the Lagrangian being optimized is close to the actual value for a given $\mathbf{q}(t)$ i.e. the Legendre transform in $\mathbf{k}$ is well approximated. A $\Delta\tau$ that is too small takes too long to converge. However, if $\Delta\tau$ is too large, the algorithm converges to a solution with a slightly higher action or in some cases is unstable. Apart from higher precision in the action, increasing the number of discretization points does not seem very helpful. Convergence is quite slow. It takes about 95k iterations to reach an action of 7.8496

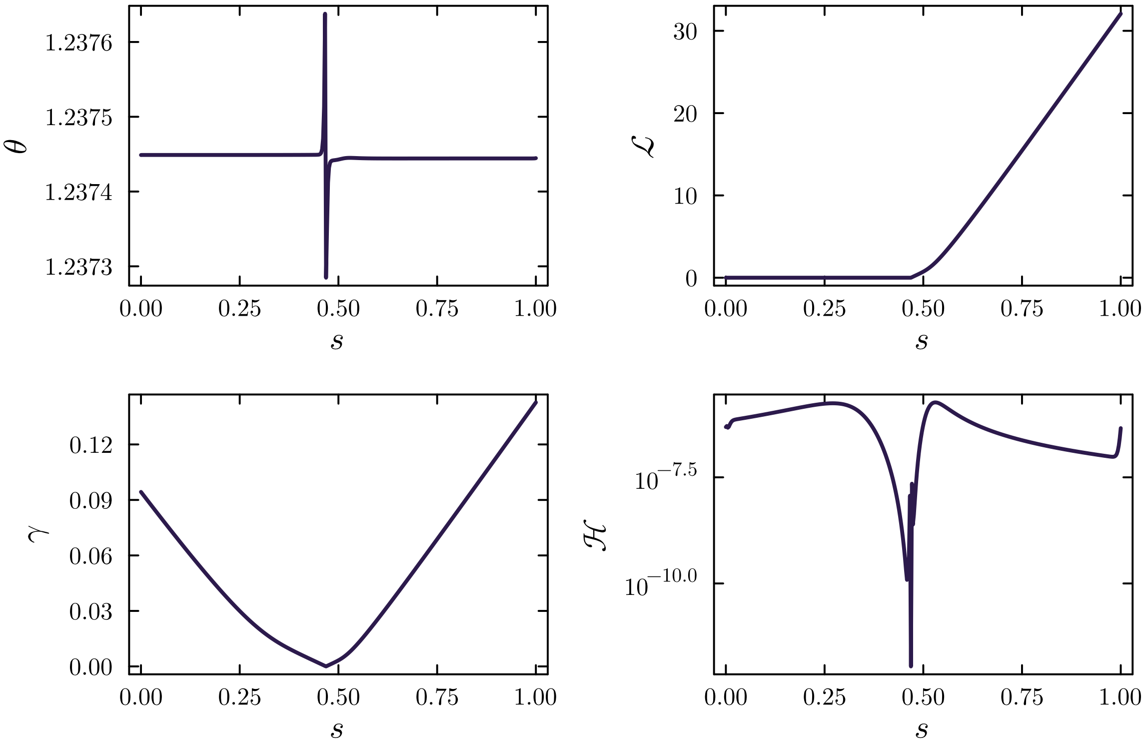

Figure 3.8: θ, γ, the Hamiltonian and the Lagrangian vs normalized path length of the persistent limit GMAM solution. The Hamiltonian is plotted on absolute log scale for clarity

It is seen in Fig. 3.8 that there is a small spike in θ at the point where the trajectory leaves C_1 (corresponding to the point where $\gamma = 0$), but it is quite small. Similar spikes can be seen in the momenta also but the scale in Fig. 3.7b obfuscates it. This is expected as the GMAM has reduced accuracy near fixed points. The Lagrangian is also small during gradient descent as expected. The Hamiltonian being zero is a good convergance criterion. It is smallest as it crosses C_1 (which also confirms that it arrives and leaves C_1 in infinite time) but is still small elsewhere.

For larger values of D_θ, the GMAM seems to have trouble leaving C_1 at the correct point, however it works fine for some initial guesses and parameter values. In Fig. 3.9, the initial guess is a parametric spline generated such that $\mathbf{r}_{guess}(0) = (0, 0)$, $\mathbf{r}_{guess}(0.5) = C_1(0.5)$ and $\mathbf{r}_{guess}(1) = (5.0, 8.16)$. The initial guess for θ vs s is linear between 0 and 0.5.

In general, the gradient descent portion of the trajectory is heavily influenced by the initial guess. This is because gradient descent trajectories are local minima of the action. Once the initial part of the trajectory is close enough to gradient descent, further changes are not seen. Instead, the algorithm prefers to diffuse across C_1 to the optimal leaving point. This is seen in Fig. 3.9a and Fig. 3.10 where the gradient descent is with $\theta = 0.5$ but the optimal leaving point is at $\theta \approx 0.6$.

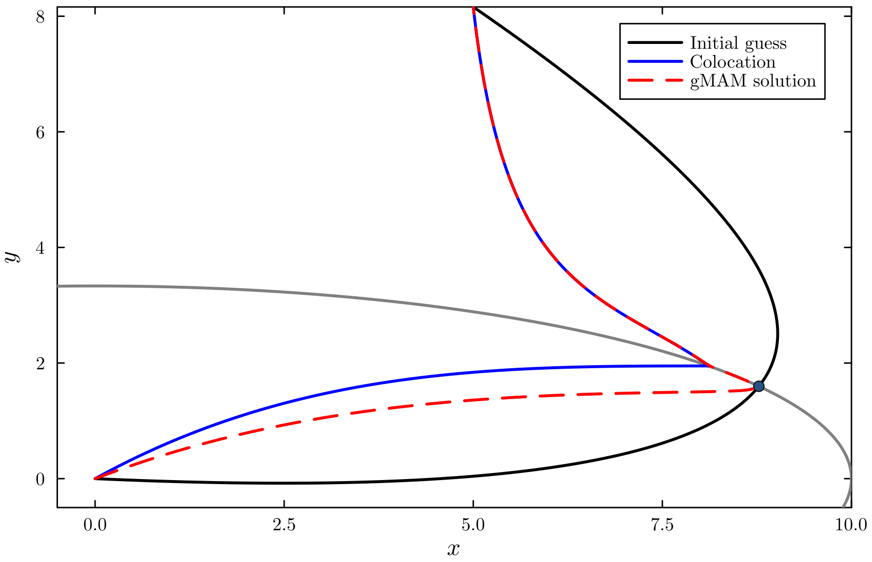

(a) x and y

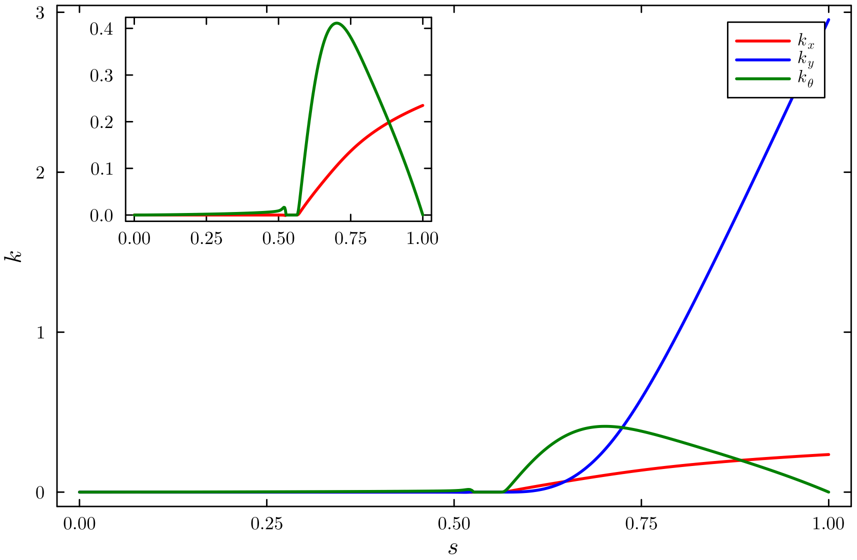

(b) k_x, k_y and k_θ. Inset only shows k_x and k_θ

Figure 3.9: GMAM solution for $D_\theta = 0.1$

The kinks in k_θ is clearly seen in Fig. 3.9b. The final action for the GMAM solution is 7.5612, and the colocation action is 7.5204. The discretized colocation action is 7.5569. This is still considerably smaller than the difference of action in the persistent limit, but they are in the same ballpark.

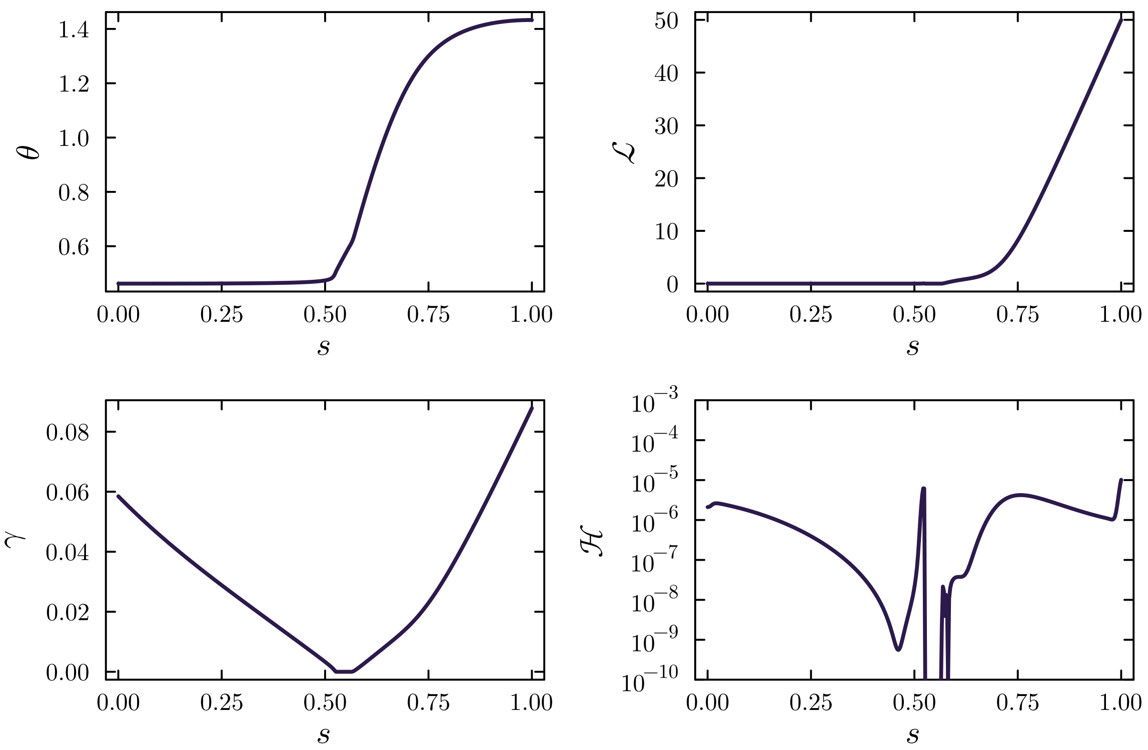

Figure 3.10: θ, γ, the Hamiltonian and the Lagrangian vs normalized path length of the GMAM solution for $D_\theta = 0.1$. The Hamiltonian is plotted on absolute log scale for clarity

Once again the Hamiltonian is very small close to the fixed point at C_1, but it is still quite small ($O(10^{-6})$) away from it too. The finite interval over which $\gamma = 0$ corresponds to the portion of the trajectory diffusing along C_1

For Fig. 3.9 and Fig. 3.10, the value of α used is of 0.5. This is because a larger α seems to allow easy diffusion across C_1. However, if α is too large, the trajectory does not "peel" off of C_1 at the right point. This depends on the optimal point on C_1 i.e, a carefully chosen value of α does not ensure that the trajectory leaves C_1 at the right point for different values of D_θ or the escape point.

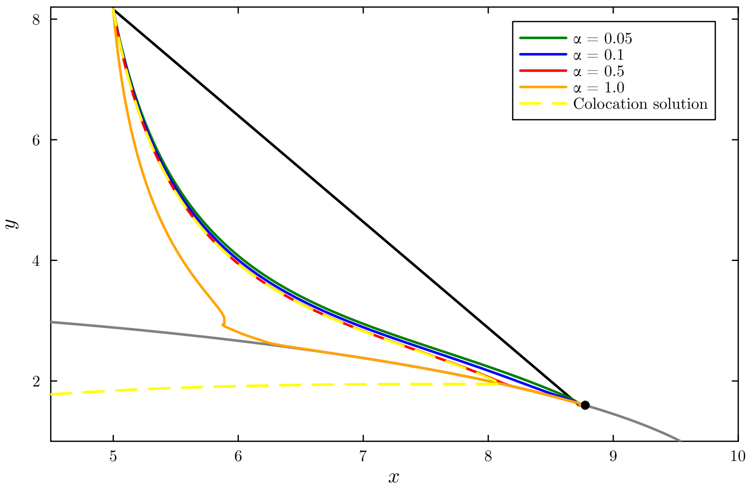

(a) x and y

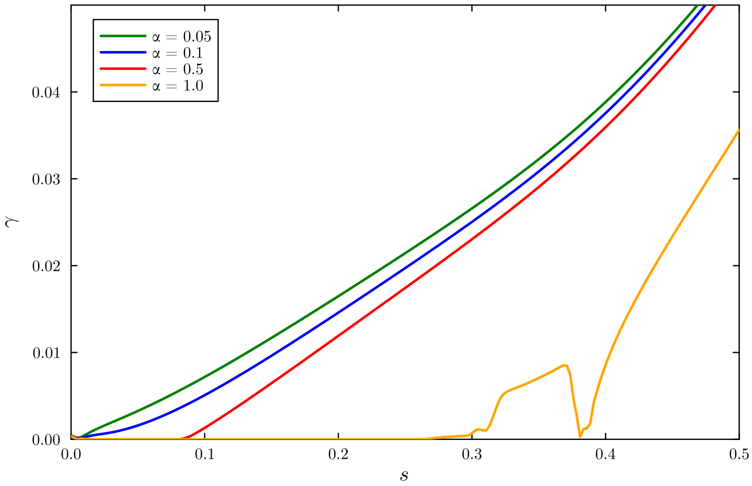

(b) Zoomed in plot of γ showing when the trajectory leaves C_1

Figure 3.11: Comparison of GMAM solutions for different α

Fig. 3.11 shows different trajectories that start from C_1 with a fixed $\theta = 0.5$. The initial guess in θ is again linear and increases to 1.25 times the original value. Fig. 3.11a shows that for small α, the solution leaves C_1 too soon but remains quite close to the collocation solution. For $\alpha = 1$, the deviation from the collocation solution is already quite large. The relative proportion of the trajectory spent on C_1 is seen in more detail in Fig. 3.11b where $\gamma = 0$ for larger s if α is larger. For $\alpha = 1.0$, we can already see strange behaviour in γ.

It is possible that the "wrong" trajectories in Fig. 3.11 are the actual minimum action paths and the collocation is only finding a stationary local minimum (or vice versa). Alternatively, it is possible that the minimum action paths are degenerate even when starting from C_1. In either case, a check is to see if the GMAM solution follows

Hamilton's equations. In the path length reparametrization it looks like this:

$$\gamma \dot{\mathbf{q}} = \nabla_{\mathbf{k}} \mathcal{H} \tag{3.19}$$

$$\gamma \dot{\mathbf{k}} = -\nabla_{\mathbf{q}} \mathcal{H} \tag{3.20}$$

Fig. 3.12a and Fig. 3.12b show $\gamma \dot{\mathbf{q}} - \nabla_{\mathbf{k}} \mathcal{H}$ and $\gamma \dot{\mathbf{k}} + \nabla_{\mathbf{q}} \mathcal{H}$ respectively. The solid lines are from the full trajectory in Fig. 3.9a. The dashed lines are from a trajectory with a linear initial guess that leaves C_1 at a suboptimal point. This trajectory is shown in Fig. 3.12c.

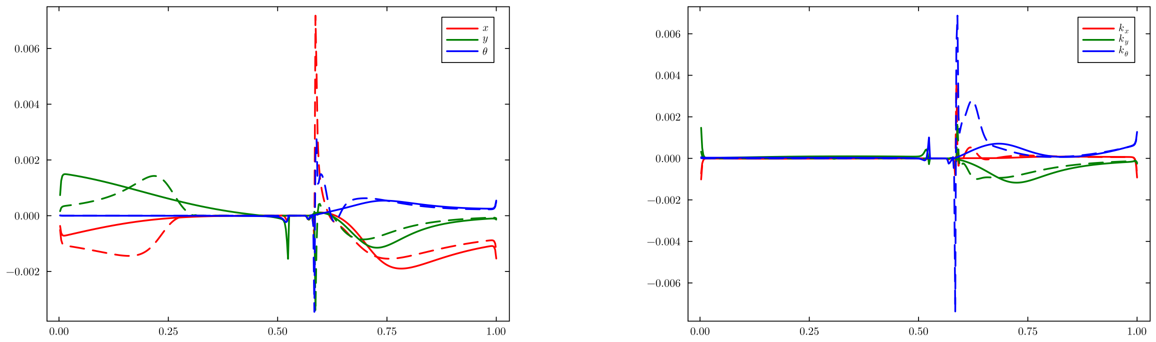

(a) $\gamma \partial_s q - \partial_k \mathcal{H}$ for different q

(b) $\gamma \partial_s k + \partial_q \mathcal{H}$ for different k

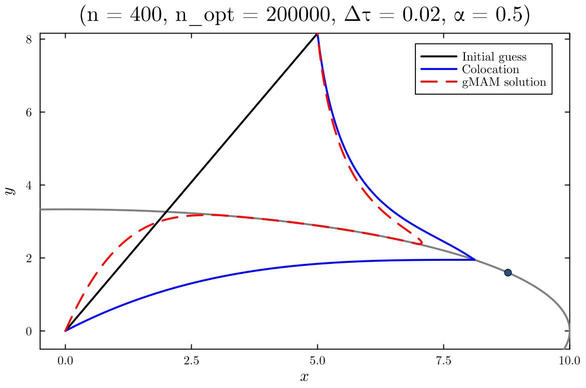

(c) Trajectory used for the dashed lines

Figure 3.12: Checking the stationarity of GMAM solutions

Both trajectories seem to satisfy Hamilton's equations to the same extent. It is possible more discretization points will improve the precision. But currently, the GMAM is not precise enough for its solutions to follow Hamilton's equations. So it will not be used as a convergence criterion.

3.3 Type-1 PSN

In studying the trajectories for non-zero λ, we first consider type-1 noise where

$$\rho(x) = \frac{1}{2}[\delta(1-x) + \delta(1+x)] \tag{3.21}$$

By setting $D_\theta \neq 0$, we can add some Gaussian noise to the self propulsion direction.

As in the 1-d case, we do not see anything qualitatively different in the presence of this tumbling motion. The particle still performs gradient descent to $C_1(\theta^*)$ followed by an instantonic escape. First, we set $D_\theta = 0$ so only the effect of tumbling motion remains. Since $\phi(x) = \sinh(x)$ is well-behaved everywhere, we expect behavior similar to the Gaussian case with $D_\theta = \lambda\sigma^2(\xi_{PSN}) = \lambda a^2$.

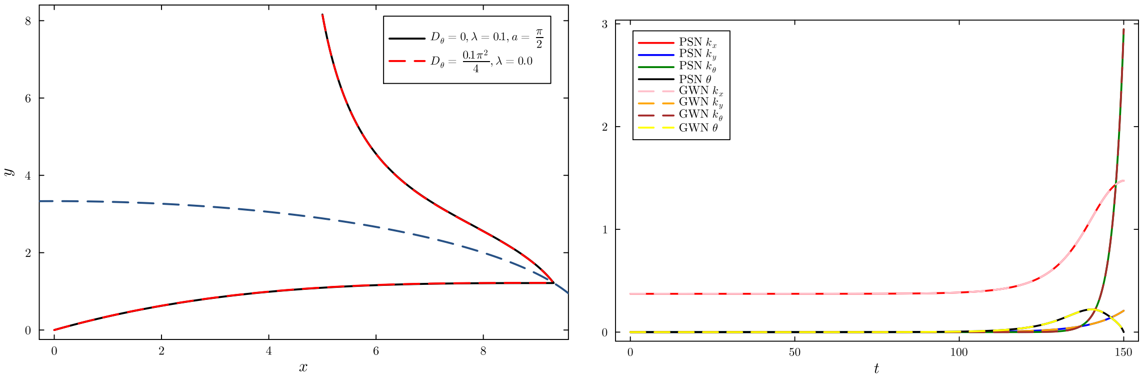

(a) Comparison of trajectories

(b) Comparison of momenta and θ

Figure 3.13: Comparison of pure run and tumble and Gaussian escape paths

This is confirmed above where the purely Gaussian and shot noise affect θ in the same way. As in the case of 1-d escape, this is because higher terms in the Taylor expansion of $\lambda\phi'(ax)$ do not have significant contribution in determining the Lagrangian. In fact, we expect the PSN to have a less significant role here. This is because there is no "potential" in θ, i.e a term in the Lagrangian of the form $k_\theta f(\theta)$. Looking only at the terms coupled to k_θ, this looks like

$$L_\theta = \max_{k_\theta} k_\theta[\dot{\theta} + f(\theta)] - \frac{D_\theta k_\theta^2}{2} - \lambda\phi(ak_\theta) \tag{3.22}$$

For any given θ, the maximization in k_θ implies that

$$D_\theta k_\theta + a\lambda\phi'(ak_\theta) = \dot{\theta} + f(\theta) \tag{3.23}$$

Supposing that $f(\theta)$ is positive like a potential gradient during barrier crossing, the right hand side of the equation is bigger. Since the LHS is increasing in θ (due to ϕ being convex), this implies that all else being equal, k_θ is smaller in the absence of f. This means that the higher order terms in ϕ' contribute less to the expansion, making the Gaussian approximation more precise.

This argument works even though S depends on θ via coupling to k_x and k_y, because that only affects the outer θ minimization of the expression in (3.22) while the above statement is true for any θ.

No significant difference is seen on setting $D_\theta \neq 0$ for most values of λ and a. The trajectory with run and tumble motion still moves as if with a $D_\theta^{eff} = D_\theta + \lambda a^2$.

The smaller impact of PSN on θ is also seen in the extent to which the non-Gaussian corrections to ϕ' affect S. In the graph below, we plot $S_r = \frac{S}{S_{GWN}}$. Here, S_{GWN} is the action for a trajectory driven only by GWN with $D_\theta = \lambda a^2$. Varying λ and a, we can see the regions in which the higher order contributions are important.

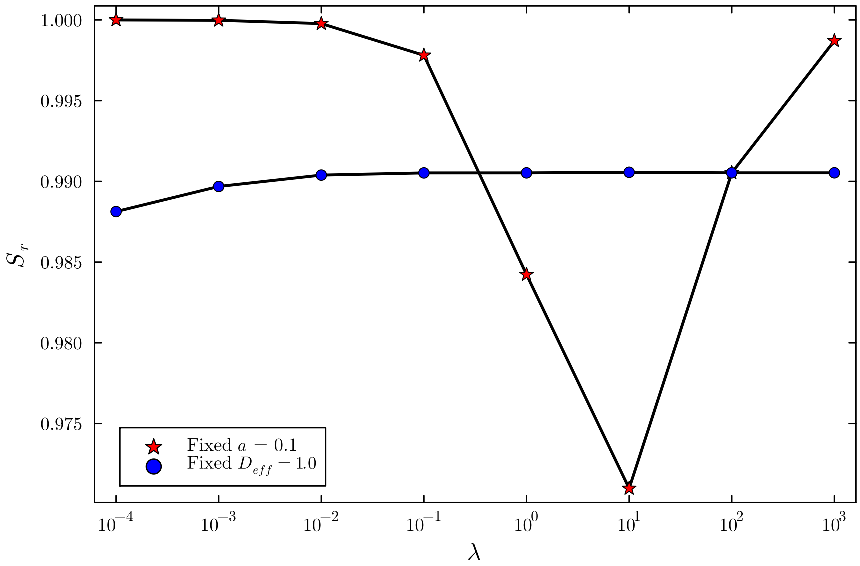

Figure 3.14: The red points have a fixed $a = 0.1$ with λ varying. The comparison is with the Gaussian trajectory with the same D_{eff}. The blue points have a fixed $D_{eff} = 0.1$. a is changed along with λ to make this constant.

As seen in [14], for a fixed a, we find maximum deviation from the Gaussian approximation for intermediate values of λ even though the extent of reduction is considerably smaller compared to the values reported there. This dependance on λ is because for small λ, the effect of the PSN as a whole on the dynamics is small. From the Hamilton's equations, it can be seen that $\dot{\theta} \to 0$ and we are in the persistent limit. To be more precise, by the same arguments as in [14], the contribution to the action from (3.22) approaches the Gaussian approximation for $\lambda \to 0$ for any given θ. Thus, for the optimal $\mathbf{q}$, the full action and the Gaussian approximation both approach the value in the persistance limit resulting in a ratio of 1.

As seen in (3.23), for a given θ, the LHS increases for larger lambda, necessitating a decrease in k_θ to maintain the equality. For small k_θ, the higher order contributions are small and the Gaussian approximation works well. This is seen in the graph as the ratio increasing back to 1 but due to numerical issues trajectories could not be obtained for λ much larger than 10^3.

The plot also shows how S_r varies on changing λ but keeping D_{eff} constant. A decrease in action is seen for small λ which is consistent as this corresponds to a higher a. For a given θ, since λa^2 remains constant any change in k_θ as λ and a varies is just due to the non-Gaussian contributions. Since they go as $\lambda O(a)^3$, they are more significant as a increases even if D_{eff} is constant.

3.3.1 Asymmetric noise

We briefly consider the effect of adding asymmetric shot noise. Note that here, even though we make ρ asymmetric with non-zero mean, $\langle \xi_{PSN} \rangle$ remains zero because we subtract the mean and redefine the noise as $\xi_{PSN} - \langle \rho \rangle$. The only modification to the Hamiltonian is that ϕ is now

$$\phi(x) = \int (e^{-xu} - ux - 1)\rho(u)\mathrm{d}u \tag{3.24}$$

The example we use is an asymmetric δ kick at ± 1 such that

$$\rho(x) = p\delta(1-x) + (1-p)\delta(1+x) \tag{3.25}$$

with $p \in [0, 1]$. The escape behavior is still qualitatively the same. The only interesting modification is that unlike D_θ, λ and a the effect of p is spatially dependent.

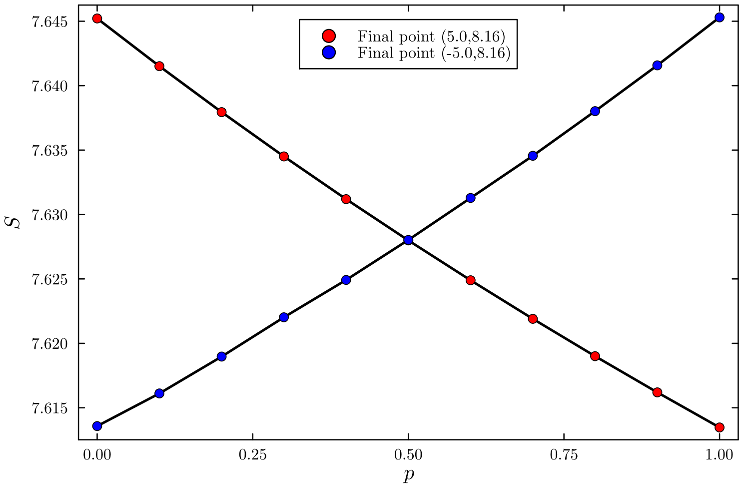

Figure 3.15: Action as a function of p for two different escape points reflected about the y axis

This is because ϕ is no longer symmetric under $k_\theta \to -k_\theta$. The addition of PSN still reduces the action because the integral in (3.24) still remains positive. The effect of higher order terms too are unchanged because all terms in (3.24) of $O(x^4)$ are unaffected by the extra term in ϕ. This asymmetry in action is present if the final points are reflected about the x axis too.

3.4 Type-2 PSN

The example of type-2 noise we consider is exponential i.e. $\rho(x) = \frac{\exp(|x|)}{4}$. In this case, ϕ has the form

$$\phi(x) = \frac{x^2}{2(1-x^2)} \tag{3.26}$$

We expect the trajectories to be smooth for finite λ as in the 1-d case[14]. The rationale for this is explained further below. Therefore, the approach of numerically solving the Hamilton's equations should still work in principle. However there are several numerical complications. The most obvious one is the singularity at ± 1. Apart from that, even though $|k_\theta|$ can physically not be greater than $\frac{1}{a}$, this is numerically imposed by the singularity in ϕ at ± 1. For small λ (where all the interesting phenomena lie), the effect of the singularity is only felt for k_θ in a very small interval around $k_\theta = \pm\frac{1}{a}$. If the solver is not precise enough it does not see the singularity and as a whole the dynamics is as if in the GWN persistent limit. The collocation method also uses a polynomial basis to find the solution so naturally any sharp increase in θ will be smoothed over.

Despite this, we have some intuition about how the persistent limit works even if numerical verification has proved problematic. Looking at the Hamilton's equations,

$$\dot{x} = v\cos\theta - \partial_x V + Dk_x \tag{3.27}$$

$$\dot{y} = v\sin\theta - \partial_y V + Dk_y \tag{3.28}$$

$$\dot{\theta} = D_\theta k_\theta + \lambda\phi'(k_\theta) \tag{3.29}$$

$$\dot{k_x} = \partial_x^2 V k_x \tag{3.30}$$

$$\dot{k_y} = \partial_y^2 V k_y \tag{3.31}$$

$$\dot{k_\theta} = k_x v\sin\theta - k_y v\cos\theta \tag{3.32}$$

The gradient descent portion of the trajectory is still unaffected as $k_\theta = 0$ inside C_1. So we are only concerned about the trajectory after it leaves from C_1. In the highly persistent limit where $D_\theta \to 0$ and $\lambda \to 0$, the particle moves as if under the influence of GWN unless $k_\theta \to \pm\frac{1}{a}$. For ease of explanation, we consider the behavior near $\frac{1}{a}$. As k_θ approaches $\frac{1}{a}$, θ increases rapidly. As observed in [14], we will see that this rapid increase approaches a jump in θ as $\lambda \to 0$. The singularity in ϕ at $\frac{1}{a}$ will again act as a cutoff preventing k_θ from increasing beyond it. For the ABP, a jump in θ corresponds to a tumble. In the case of a harmonic potential, since $\partial_x^2 V$, $\partial_y^2 V$ are constant, k_x and k_y increase at an exponential rate independent of other variables. Thus for k_θ sufficiently close to $\frac{1}{a}$, k_x and k_y are approximately constant. This causes (3.30) and (3.32) to be uncoupled from the other equations.

Defining $A = v\sqrt{k_x^2 + k_y^2}$, $\alpha = \arctan(\frac{k_y}{k_x})$, $\Theta = \theta - \alpha$, and setting $D_\theta = 0$, (3.30) and (3.32) are of the form

$$\dot{\Theta} = \lambda \phi'(k_\theta) \tag{3.33}$$

$$\dot{k_\theta} = A \sin\Theta \tag{3.34}$$

The flow of these equations are given below

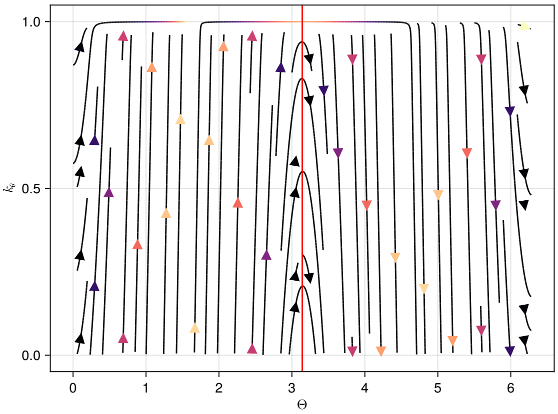

Figure 3.16: The flow of (3.33) and (3.34) for $\lambda = 10^{-3}$. The red line is $\theta = \pi$

From Fig. 3.16, it can be seen that for k_θ close to the cutoff and $\Theta < \pi$, k_θ first increases causing an increase in Θ. As Θ increases beyond π, k_θ starts reducing. $\dot{\Theta}$ is non-zero until k_θ moves a finite distance away from the cutoff further increasing Θ to a final value $\Theta_f = 2\pi - \Theta_i$. This behavior is seen in the example solution shown below in Fig. 3.17.

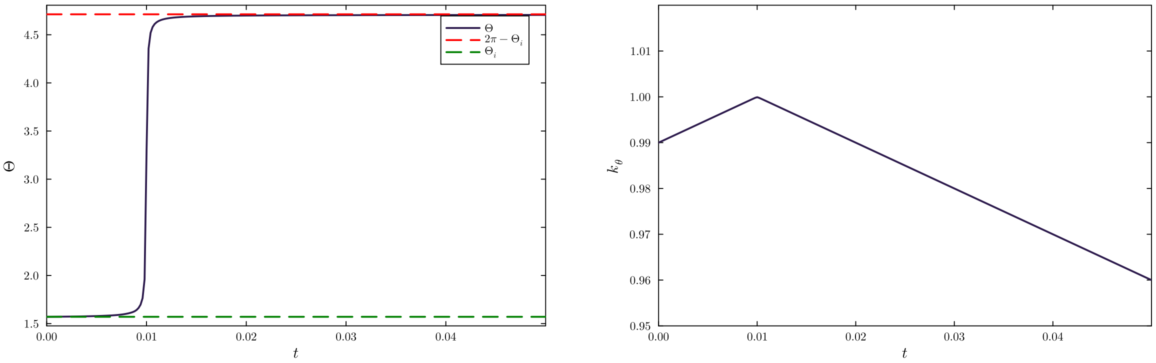

(a) Θ vs t. The reflection around π is clearly seen

(b) k_θ vs t. k_θ also seems to be reflected arount $t = t_c$ where it is closest to the cutoff

Figure 3.17: Solution to the initial value problem described by the system of ODEs given above with $a = 1$ and $\lambda = 10^{-3.5}$

This behavior of Θ reflecting can be explained as follows: Suppose we consider $\dot{\Theta}$ to be significant when $\phi'(k_\theta) > \frac{1}{\lambda}$, and k_θ is sufficiently close to the singularity for this to be true if $\frac{1}{a} - k_\theta < \varepsilon$. For small λ and k_θ outside this region, $\lambda\phi'(k_\theta) \approx 0$ except in a small region that shrinks with λ. We start with $\frac{1}{a} - k_\theta(t_i) < \varepsilon$ and $\Theta^i < \pi$. Since k_θ starts decreasing a finite distance away from $\frac{1}{a}$, we set $k_\theta(t_f) = k_\theta(t_i)$ as Θ remains constant for $t > t_f$. We know that k_θ decreases below $k_\theta(t_i)$ because we are only interested in trajectories where k_θ decreases to 0. Since $\varepsilon \to 0$ in the persistent limit, it can be made small enough such that $\dot{\theta} >> \dot{k_x}$ and $\dot{k_y}$ for $t \in [t_i, t_f]$. Since k_θ never hits the cutoff, everything is smooth. So the equations for Θ and k_θ can be rewritten using the chain rule and integrated as shown below.

$$\lambda \phi'(k_\theta)\dot{k}_\theta = A\sin(\Theta)\dot{\Theta} \tag{3.35}$$

$$\lambda[\phi(t_f) - \phi(t_i)] = -A[\cos(\Theta_f) - \cos(\Theta_i)] \tag{3.36}$$

$$\cos(\Theta_f) = \cos(\Theta_i) \tag{3.37}$$

$$\theta_f = 2\pi\mathbb{Z} - \theta_i + 2\alpha \tag{3.38}$$

Since k_θ is symmetric about the time when it is closest to the cutoff (as seen from Fig. 3.17b), $t_f - t_i \to 0$ along with ε. Thus there is an infinitesimal interval of time during which θ jumps from θ^i to θ^f and outside which it remains constant. From the family of possible values for θ^f, we choose the smallest θ^f such that $\theta^f > \theta^i$, as $\dot{\theta} > 0$. Physically, (3.36) is equivalent to the fact the $\mathcal{H}$ is constant throughout the trajectory.

Returning to the full set of Hamilton's equations and setting $t = 0$ as the point where jump occurs, the solutions for $t < 0$ in the persistent limit are

$$x^i(t) = \frac{v\cos(\theta^i)}{\lambda_x} + \frac{k_x(0)D}{2\lambda_x}\exp(\lambda_x t) - \left(\frac{v\cos(\theta^i)}{\lambda_x} + \frac{k_x(0)D}{2\lambda_x} - x(0)\right)\exp(-\lambda_x t) \tag{3.39}$$

$$y^i(t) = \frac{v\sin(\theta^i)}{\lambda_y} + \frac{k_y(0)D}{2\lambda_y}\exp(\lambda_y t) - \left(\frac{v\sin(\theta^i)}{\lambda_y} + \frac{k_y(0)D}{2\lambda_y} - y(0)\right)\exp(-\lambda_y t) \tag{3.40}$$

$$\theta(t) = \theta^i \tag{3.41}$$

$$k_x(t) = k_x(0)\exp(\lambda_x t) \tag{3.42}$$

$$k_y(t) = k_y(0)\exp(\lambda_y t) \tag{3.43}$$

$$k_\theta^i(t) = \frac{v\sin(\theta^i)k_x(0)}{\lambda_x}(\exp(\lambda_x t)) - \frac{v\cos(\theta^i)k_y(0)}{\lambda_y}(\exp(\lambda_y t)) \tag{3.44}$$

Since we want the solutions to remain finite for $t \to -\infty$,

$$x^i(0) = \frac{v\cos(\theta^i)}{\lambda_x} + \frac{k_x(0)D}{2\lambda_x} \tag{3.45}$$

$$y^i(0) = \frac{v\sin(\theta^i)}{\lambda_y} + \frac{k_y(0)D}{2\lambda_y} \tag{3.46}$$

Notice that $(x^i(t), y^i(t)) \to C_1(\theta^i)$ for $t \to -\infty$ as expected since we have gradient ascent away from the cutoff. Additionally, since $k_\theta^i(0) = \frac{1}{a}$ we have the condition

$$\frac{v\sin(\theta^i)k_x(0)}{\lambda_x} - \frac{v\cos(\theta^i)k_y(0)}{\lambda_y} = \frac{1}{a} \tag{3.47}$$

For $t > 0$, $\theta(t) = \theta^f$. Since k_x and k_y remain smooth through the cutoff, this means that the coefficient of $\exp(-\lambda_x t)$ and $\exp(-\lambda_y t)$ in (3.40) and (3.41) are non-zero. So the positional coordinates no longer perform gradient ascent. We also want $k_\theta^f(0) = \frac{1}{a}$. With these considerations, the solutions for $0 < t < t_f$ are modified as

$$x^f(t) = x^i(t) + \frac{v}{\lambda_x}[\cos(\theta^f) - \cos(\theta^i)](1 - \exp(-\lambda_x t)) \tag{3.48}$$

$$y^f(t) = y^i(t) + \frac{v}{\lambda_y}[\sin(\theta^f) - \sin(\theta^i)](1 - \exp(-\lambda_y t)) \tag{3.49}$$

$$k_\theta^f(t) = \frac{v\sin(\theta^i)k_x(0)}{\lambda_x}[\exp(\lambda_x t) - 1] - \frac{v\cos(\theta^i)k_y(0)}{\lambda_y}[\exp(\lambda_y t) - 1] + \frac{1}{a} \tag{3.50}$$

$$\theta^f(t) = \theta^f \tag{3.51}$$

In (3.51), θ^f is obtained by reflecting the Θ^i corresponding to θ^i about π. t_f is defined by $k_\theta(t_f) = 0$. Note that equations (3.40)-(3.51) assume a trajectory with exactly one jump. This adds the inequality constraint $|k_\theta(t)| < \frac{1}{a}$ for $t \neq 0$

We proceed with calculating the action of such a trajectory. For $t < 0$, the motion is just gradient ascent so the associated action cost is just the cost of passively climbing the effective potential difference between $C_1(\theta^i)$ and $(x(0), y(0))$ with the self propulsion direction fixed to θ^i. For $t > 0$, the particle no longer performs gradient ascent. Keeping in mind the fact that $\dot{\theta} = 0$ and $\lambda\phi'(k_\theta) = 0$ beyond the cutoff, it can be seen that for $\mathbf{q}, \mathbf{k}$ that are solutions of Hamilton's equations, the Lagrangian is of the form $\mathcal{L} = \frac{D}{2}(k_x^2 + k_y^2)$

Since k_x and k_y are smooth across the jump, the post-jump Lagrangian can be found by just continuing the pre-jump trajectory for $t > 0$. Equivalently, the contribution to the Lagrangian associated with the deviation from gradient ascent (x^i, y^i) in (3.48) and (3.49) is 0. Thus, the action from the "continuous" portions of the trajectory is just

$$S_{cont} = \frac{2}{D}[V_{eff}(x^i(t_f), y^i(t_f), \theta^i) - V_{eff}(C_1(\theta^i))] \tag{3.52}$$

Next, we calculate the action cost associated with the jump. As in the 1-d case in [14], we expect it to be of the form $\theta_f - \theta_i$. Unlike the 1-d, case we have no potential term in θ. So, in the persistent limit, we can calculate the Legendre transform in θ explicitly. Suppose $|\dot{\theta}| > 0$. For simplicity, we assume $a = 1$. The maximization in k_θ

gives

$$\dot{\theta} = \lambda\phi'(k_\theta) \tag{3.53}$$

$$\dot{\theta} = \lambda\frac{k_\theta}{1-k_\theta^2}\left(1+\frac{k_\theta^2}{1-k_\theta^2}\right) \tag{3.54}$$

$$(1-k_\theta^2)\dot{\theta} = \lambda k_\theta\left(1+\frac{k_\theta^2}{1-k_\theta^2}\right) \tag{3.55}$$

$$(1-k_\theta^2)\frac{k_\theta}{2}\dot{\theta} = \underbrace{\frac{\lambda}{2}\left(\frac{k_\theta^2}{1-k_\theta^2}\right)}_{\lambda\phi(k_\theta)} \tag{3.56}$$

From (3.56) it can be seen that if k_θ does not approach ± 1 as $\lambda \to 0$ the LHS remains non-zero whereas the RHS does not. This also shows that $|\dot{\theta}| > 0$ in some sense requires $k_\theta^2 = 1$ i.e. θ can only change near the cutoff. If $k_\theta \to \pm 1$, it is required that the second term in the RHS of (3.56) (which is just $\lambda\phi(k_\theta)$) go to zero like the LHS. There still remains the choice of ± 1 for the limiting value. Notice that the RHS is always positive. Thus if $\dot{\theta} < 0$, $k_\theta \to -1$ and if $\dot{\theta} > 0$, $k_\theta \to 1$. So, the terms in the Lagrangian that are affected by the jump behave as

$$\max_{k_\theta} k_\theta\dot{\theta} - \lambda\phi(ak_\theta) \to \frac{|\dot{\theta}|}{a} \tag{3.57}$$

So far, we have not really considered the fact that θ is periodic. This was not relevant for Gaussian escape as θ never changed sufficiently to loop back around the principle interval. On the face of it, it is not obvious if it should be so here. For certain values of α, it seems plausible that the final angle can exceed 2π even if the initial angle lies in the principle interval. Since all 2π separated values are physically the same, we take $\theta_f \mod 2\pi$ to minimize the jump action and for consistency. In practice, this is done by first setting $\theta^f \mod 2\pi$ and

$$S_{jump} = \frac{1}{a}\min(|\theta_f - \theta_i|, 2\pi - |\theta_f - \theta_i|) \tag{3.58}$$

Numerical verification with the collocation method has proved challenging as mentioned before. Fig. 3.18 shows some examples of collocation solutions in the persistent limit. We first find a trajectory for which k_θ exceeds the cutoff if $\lambda = 0$. Then we set $\lambda = 10^{-2}$ and decrease it to observe increasingly sharper jumps in θ. We find that the solver converges for $\lambda \geq 10^{-4}$. Making the cutoff smaller, we find that the solution does not see the singularity i.e. it increases beyond the cutoff. It is seen that k_θ doesn't really reflect about t_c as expected and even though there is a fast increase in θ as k_θ closes the cutoff, this is over timescales of $O(1)$ or $O(10)$. Compared to Fig. 3.17 this is 1 or 2 orders of magnitude larger.

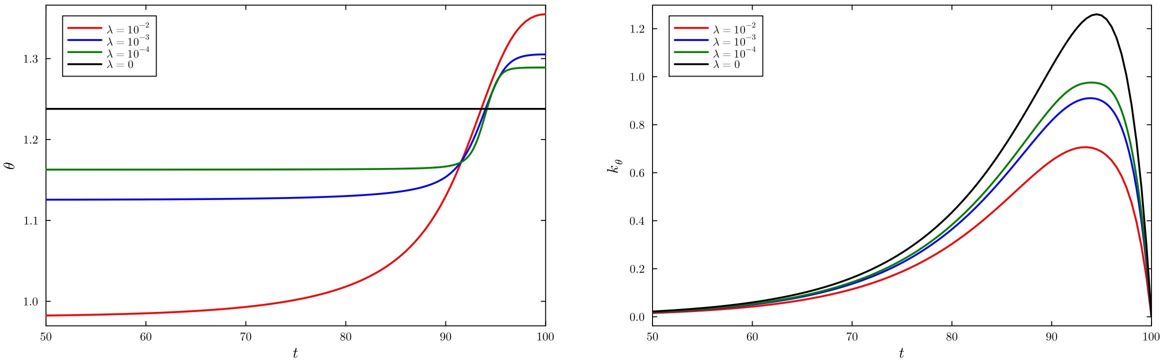

(a) θ vs t for different λ. Interestingly, the jump hieght also seems to be getting smaller.

(b) k_θ vs t. The cutoff effect is seen but the solver is not precise enough to show the reflecting behavior

Figure 3.18: Collocation solutions for type-2 PSN with different λ

Evidently, the collocation method is insufficient in this regime. A general solution for the boundary value problem is not easy to find analytically. However, using the reasoning above we can find the escape path for a fixed choice of $k_x(0)$ and θ^i. $k_y(0)$ can be found by the condition that $k_\theta(0^-) = \frac{1}{a}$. Using these, θ_f can be found by the reflecting argument and t_f by finding the first time that $k_\theta(t) = 0$ for $t > 0$ (if it does at all). All other relevant quantities can now be found using equations (3.40)-(3.56). There are some additional constraints like ensuring that the final point is uphill relative to the jump point, that the trajectory does no intersect C_1 and that there are not other points where k_θ hits the cutoff. An example solution from such a procedure is shown in Fig. 3.19.

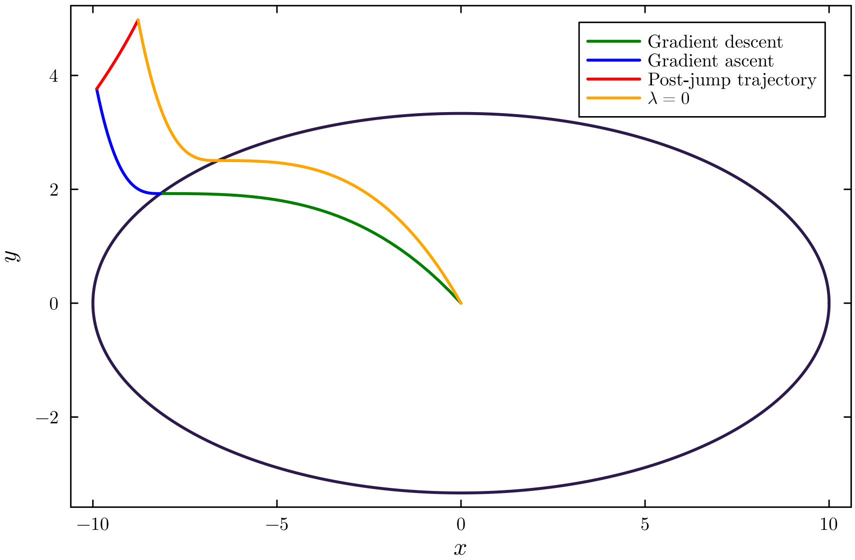

(a) The jump trajectory compared to the persistent limit solution

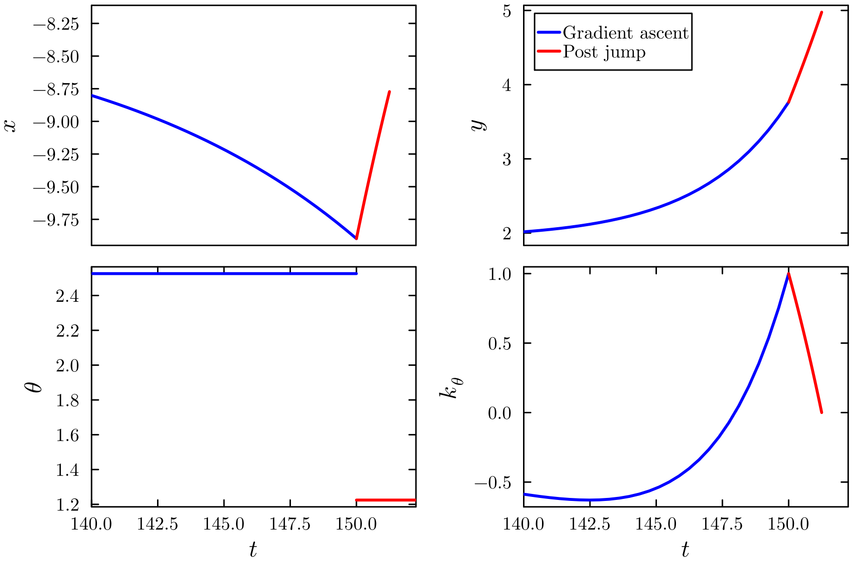

(b) Trajectory properties for the jump solution. Since k_x and k_y are simple exponentials, they have not been plotted.

Figure 3.19: An example of a jump trajectory with $k_x(0) = -0.34$ and $\theta^i = 2.52$, $a = 1$

Fig. 3.19a shows that a jump in θ corresponds to a sharp turn in the path reflected as a kink in x and y. The pre-jump portion of the trajectory does gradient ascent with a different θ compared to the persistent limit solution. It is seen from Fig. 3.19b that θ jumps to a lower value even though k_θ hits the cutoff at 1. This is a consequence of periodicity in θ. These are all general features that are expected to be seen in a typical jump trajectory. Contrary to the argument that the PSN reduces the Lagrangian, the jump trajectory has a *higher* action than the persistent limit solution. As we see below in Fig. 3.20, this is a general feature of all jump trajectories obtained by this method. It seems that the argument for the persistent limit action being lower (or at least equal) to the value for $\lambda = 0$ is fairly airtight. Presumably there is some error in either the numerics or the calculation of the jump trajectories. It is unclear as of now where exactly the problem lies. There is of course a possibility that the choice of $k_x(0)$ and θ^i is suboptimal. To test this, we find the final point and action for a jump trajectory with a particular choice of $k_x(0)$ and θ^i and compare it to the action of the optimal trajectory to that point for $\lambda = 0$. Varying $k_x(0)$ and θ^i gives different possible jump trajectories.

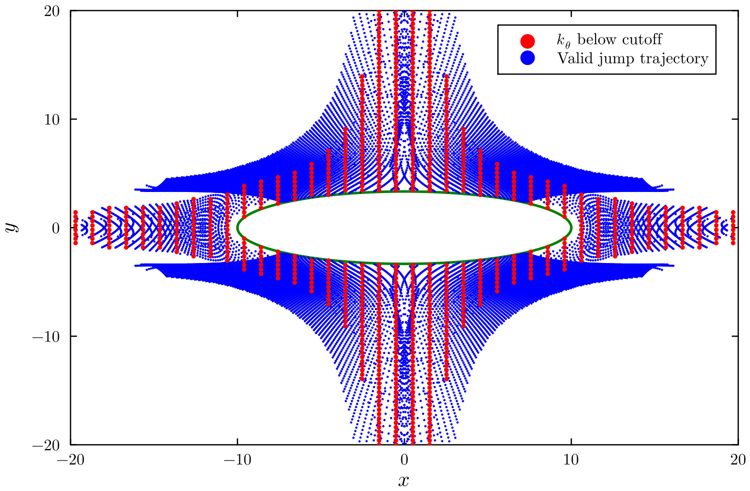

Figure 3.20: The blue points have valid jump trajectories that end there. The red points have trajectories that do not hit the cutoff (obtained by collocation method after setting $\lambda = 0$)

None of the blue points in Fig. 3.20 have a jump trajectory that is more efficient than one driven by GWN. The jump has an $O(1)$ action cost, which is not offset by lower action for the continuous portion of the trajectory. In fact, removing the jump cost there are several trajectories where the jump is preferred. It is also strange that most of the plane (the regions not covered by the red or blue points) seems inaccessible to the particle. While k_x and θ^i are not the best choice to parametrize final points, these features remain even for finer grid spacing over larger intervals. Another possibility is that most points on the plane are simply not accessible with just 1 jump. We have not considered this case in detail yet.

While there are some important issues with our analysis, some intuition about the escape behavior can still be gleaned from this. Firstly, unlike the 1-d case where the trade-off is between a jump cost and the cost of a continuous climb, here the balance is between a continuous climb and a continuous climb with a sharp turn and an added jump cost. Also, in 1-d a jump always takes the particle towards the final point. Here, it is not obvious where the self propulsion points after the jump and if it should be pointing towards the "optimal" direction.

3.5 GMAM solutions - Double well

The double well defined in Section 2.1 has minima at $\mathbf{r}_1 = (0, -1)$ and $\mathbf{r}_2 = (0, 1)$, and a saddle at (0,0). Because of the double well structure, the effective potential has three sets of fixed point contours shown in Fig. 3.21. Keeping with the earlier notation, we will call C_1 the contour enclosing the initial point at the bottom of one well, within which the particle can move with zero action cost. The particle starts in C_1 at (0,-1). The black coloured contour around the saddle point at (0,0) is called

C_2. Once the particle passes C_2, the potential is sufficiently flat that the effective potential is downhill. For $y > 0$ and outside C_2, the potential of course has a negative y directional derivative, allowing gradient descent motion in the y direction. Within C_3, the contour around $(1, 0)$, there can be a non-zero Lagrangian depending on how θ behaves. The final point lies in C_3 at (1,0). Typically one considers the particle "escaped" once it has cleared the barrier so the (relatively small) cost associated with movement in C_3 can be neglected.

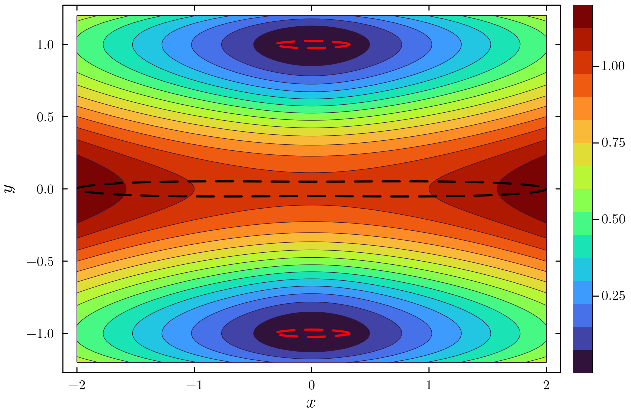

Figure 3.21: The particle can move within the dashed elliptical contours purely by orienting the self propulsion in a proper direction with zero action cost.

3.5.1 Symmetric and Asymmetric trajectories

In the absence of activity, the particle prefers to move along the straight line between $\mathbf{r}_1$ to $\mathbf{r}_2$ as any movement on the x-axis has an additional action cost. The action for this path is simply $\frac{2}{D}[V(0,0) - V(\mathbf{r}_1)]$ as it climbs up the barrier to (0,0) and then moves downhill. With activity, the symmetric trajectory is the same, where the particle is pointed at an angle $\frac{\pi}{2}$ at all times and climbs a reduced effective potential from the point on C_1 corresponding to $\frac{\pi}{2}$ to the similar point on C_2. For small values of D_θ and v_0, the particle follows the symmetric trajectory. For larger values of D_θ, it can reorient its self propulsion fast enough that it follows a different path. If v is large enough, the effective potential landscape is such that it is advantageous to move along the x axis first with $\theta = 0$.

Fig. 3.22 shows an example of a symmetric and an asymmetric trajectory.

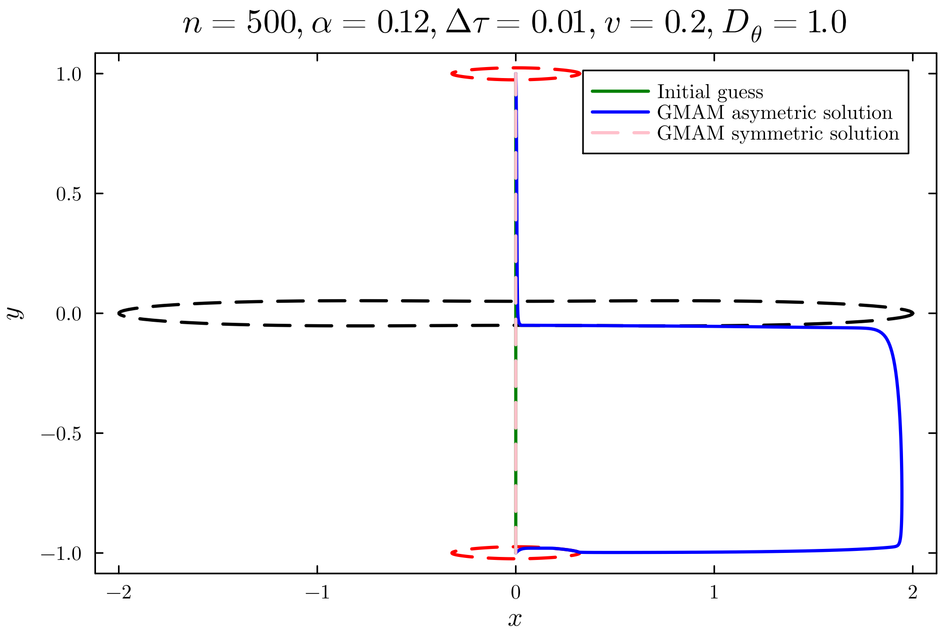

Figure 3.22: Symmetric vs Asymmetric trajectories. The symmetric trajectory was obtained by setting $D_\theta = 10^{-6}$ and an constant initial angle of $\frac{\pi}{2}$. The asymmetric trajectory had an initial guess for the angle that is linear between 0 and $\frac{\pi}{2}$ The action values are 1.6151 and 1.4386 respectively.

An intuition for these 2 types of trajectories and their D_θ/v dapendent preference is as follows. For $y \in (-1.0, 0.0)$ the gradient along y has a maximum at $y = 0$ and 2 minima as shown in Fig. 3.23.

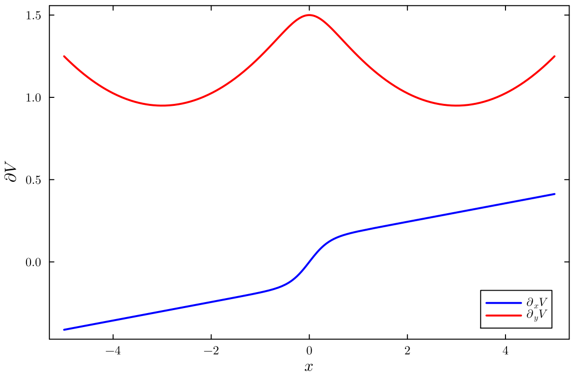

Figure 3.23: a slice of $\partial_x V$ and $\partial_y V$ vs x for $y = -0.5$

For the particle to be considered escaped, it has to cross the barrier along y. This is less steep away from $x = 0$. Thus, the action associated with this barrier crossing is reduced by moving away from $x = 0$. However, $\partial_x V$ (shown in Fig. 3.23) has a stable fixed point on the x axis for $y < 0$. Thus there is an action cost associated with climbing along the x direction till the barrier height along y is sufficiently reduced. There is also a cost to maintain this value of x since the potential gradient tends to push the particle towards $x = 0$. It is the interplay between these costs that ultimately determines which path is better.

For small D_θ and v, these costs are too high and the symmetric path is preferred.

For large D_θ, the self propulsion direction can be changed sufficiently quickly with minimal cost to make the asymmetric path preferable. As seen from Fig. 3.23, the $\partial_y V$ is much larger than $\partial_x V$. This is true for points below C_2 with x coordinate lying between the minima of $\partial_y V$. The potential is constructed such that for large enough v, the reduction in y-ward barrier height obtained by moving along the x-axis with $\theta = 0$ is sufficient to compensate for the action cost of the x-ward climb. Keeping the self propulsion pointed in the x direction also ensures that the cost of maintaining an $x > 0$ during the barrier crossing is lower. So even in the persistent limit, for v larger than a cutoff value, it is preferable to move along the asymmetric trajectory with fixed $\theta = 0$. Because of numerical issues with the GMAM, the persistent limit behaviour is not studied in the present work.

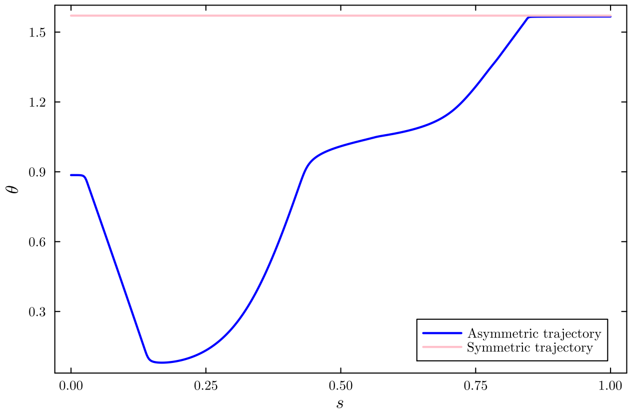

Figure 3.24: θ vs s

Since the x axis is normalized path length in Fig. 3.24, it is slightly harder to compare it to θ along the trajectory but regions where θ is linear roughly corresponds to quasi-static motion. This can be confirmed by comparing with γ vs s shown in Fig. 3.25.

It can be seen that after diffusing along C_1 quasi-statically, the particle leaves it with $\theta \approx 0$ to effectively climb the potential along x.

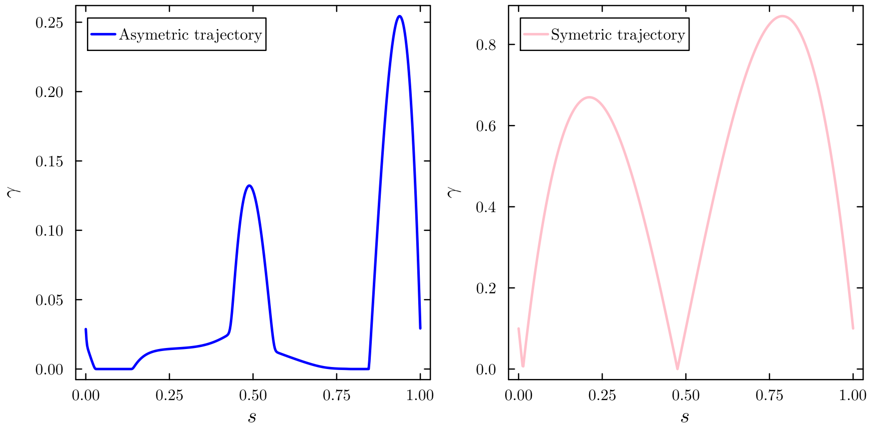

Figure 3.25: γ vs s

For the asymmetric trajectory, the initial segment where $\gamma = 0$ corresponds to quasi-static movement along C_1 to re-orient θ towards the x axis. The segment close to $s = 0.75$ corresponds to quasi-static movement along C_2 to orient θ along the y axis. The symmetric trajectory consists of a gradient descent to C_1, ascent to C_2 and finally a descent to C_3 with constant θ. Since $C_3(\pi/2)$ is located above $\mathbf{r}_2$, it can still perform gradient descent within C_3. This final portion is the same for both symmetric and asymmetric trajectories.

This is also reflected in the momenta and Lagrangians of the trajectories. For the symmetric case, only k_y is ever non zero while crossing the barrier along the y axis. For the asymmetric case, there is an initial increase in k_x to climb the well along the x axis, and subsequent decrease on return to the y axis, paired with a non-zero k_θ and k_y because of changing self propulsion direction and climbing the barrier. The smaller hump in k_y is reflective of the decreased barrier height.

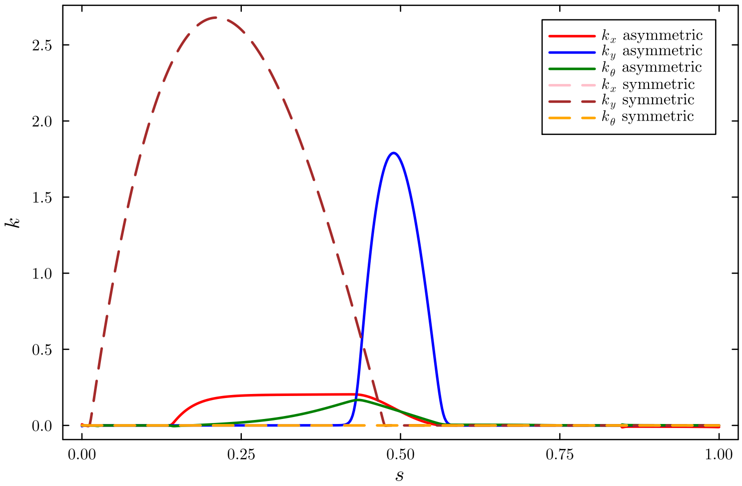

Figure 3.26: Comparison of momenta of the symmetric and asymmetric trajectories

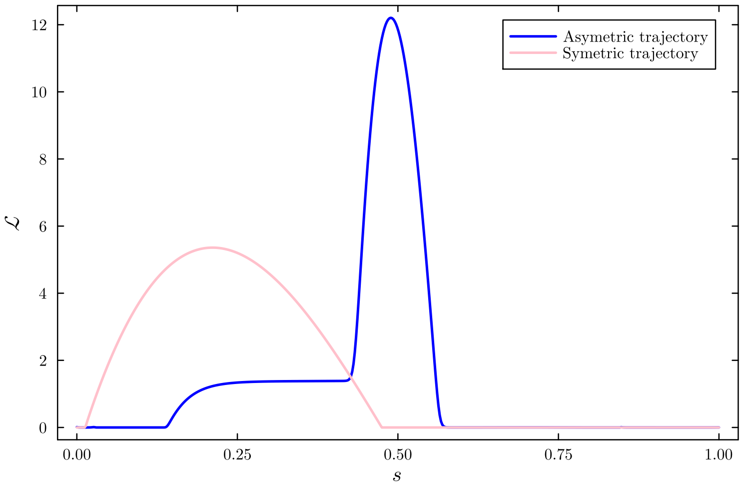

Figure 3.27: Comparison of Lagrangians of the symmetric and asymmetric trajectories

The initial hump in the Lagrangian of the asymmetric trajectory shown in Fig. 3.27

corresponds to the climb along x axis. The action cost for crossing the barrier is spread over a narrower interval for the asymmetric trajectory. This is an effect of the fact that θ and x are varying quite a lot, resulting in the increase in y accounting for a relatively small proportion of the total path length. The higher peak is also reflective of this fact since $\dot{y}(s)$ is bigger.

Now that features of the two distinct escape paths have been described, we will study the dependence of the preference between them on various parameters. Although this is only described qualitatively in the present work, there is numerical and analytical evidence to suggest that the switch in transition path from symmetric to asymmetric is a genuine phase transition.

3.5.2 Varying D_θ for a fixed v

Since there are trajectories with appreciably lower actions that use a qualitatively different escape strategy, it is worth checking how this transition happens. To test this, the parameters of the potential are the same as before. v_0 is set as 0.1 and D_θ is varied as shown. The symmetric trajectory has an action of 1.8036. If the action of the asymmetric path is lower than that of the symmetric path by more than 10^{-2} we consider it the preferred transition path.

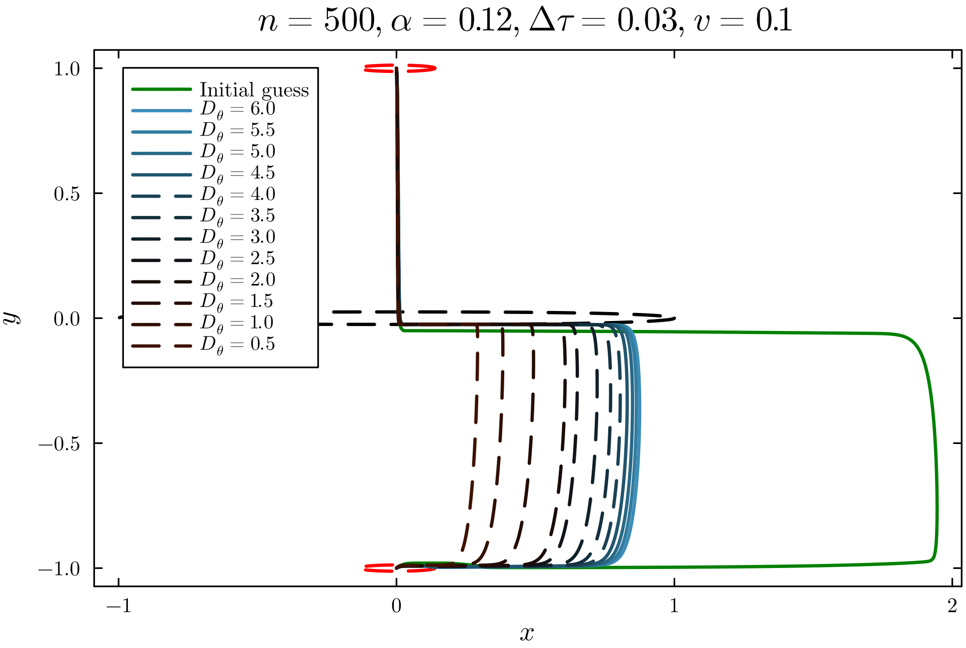

Figure 3.28: Trajectories for different D_θ. The initial guess shown in green is the result for $v_0 = 0.2$ shown above. The dashed trajectories do not have a sufficiently lower action to be preferred over the symmetric trajectory.

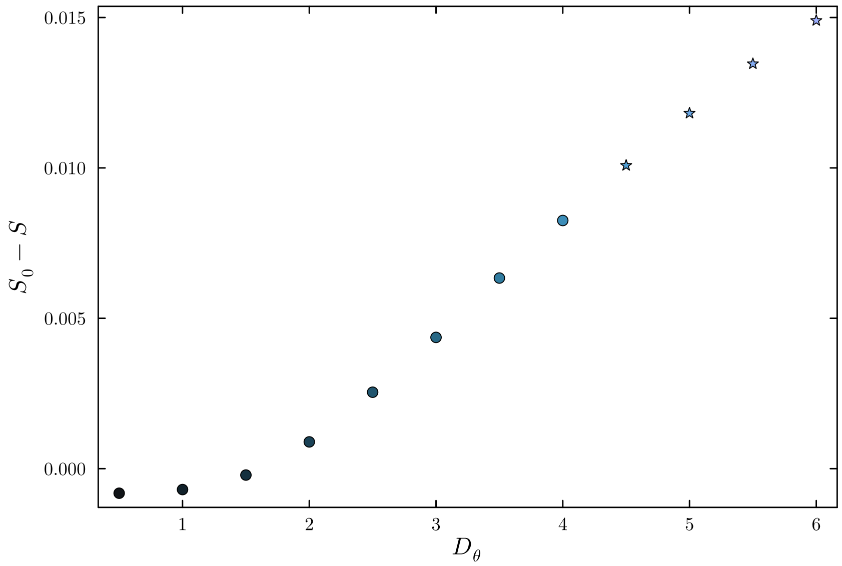

Figure 3.29: Difference between the symmetric and asymmetric actions. The starred value are significant.

The symmetric path is a stationary point of the action for any value of D_θ since it always satisfies Hamilton's equations independent of D_θ. Thus, starting with a straight line initial guess for (x, y) and constant $\pi/2$ will not result in asymmetric trajectories. Moreover, the action is a very flat function in trajectory space for smaller values of D_θ. There are trajectories that are different from both the symmetric and asymmetric path that have an action very similar to both. To bias the algorithm to explore trajectories similar to the asymmetric path, the initial guess is an asymmetric trajectory for a different parameter value.

Unlike the case of the harmonic potential, the escape path does not vary continuously with D_θ here. The GMAM cannot distinguish paths that have an action that differ by less than 10^{-2}, so we consider an action difference of 10^{-2} or more as significant. The rationale behind this is explained in Section 3.5.5

3.5.3 Varying v for a fixed D_θ

The preference between symmetric and asymmetric paths depend also on v. We set $D_\theta = 0.5$ and vary v. For small $v \leq 0.1$ we expect the symmetric trajectory to be preferred and on increasing v the preference is switched since even for small D_θ (in fact an asymmetric path is preferable even in the persistent limit). Note that unlike D_θ, v has a finite range it can vary over as if it is too large, the particle can just perform gradient descent to the final point with zero action.

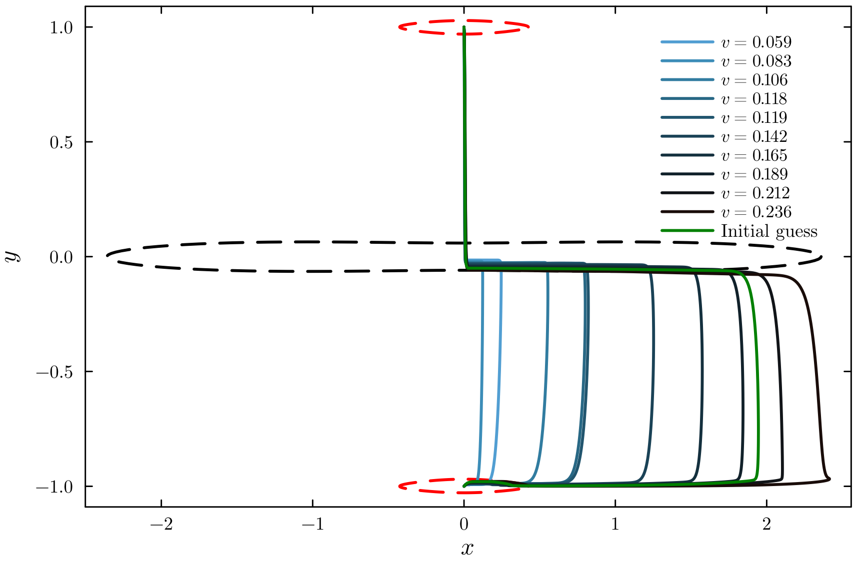

Figure 3.30: Trajectories for different vs. The C_is plotted are for the largest value $v = 0.236$

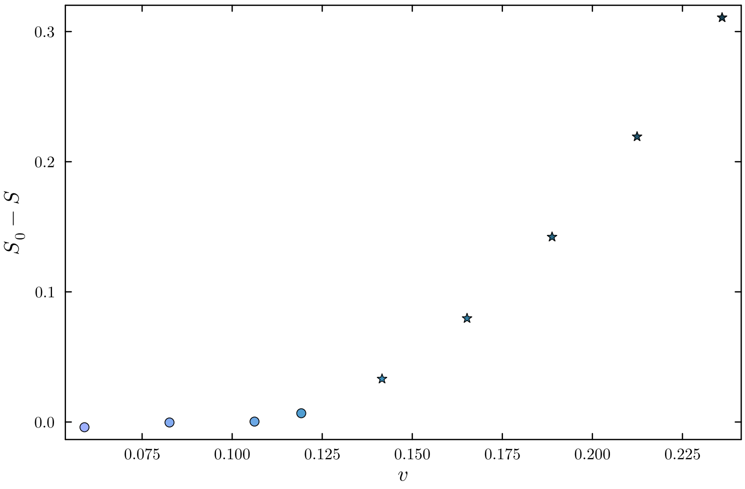

Figure 3.31: For each of the trajectories, the action difference between the symmetric trajectory corresponding to that value of v_0 and the asymmetric action is plotted

As expected, the asymmetric trajectory is preferred for larger vs. In Fig. 3.31, the symmetric action is calculated using the effective potential difference between $C_2(\frac{\pi}{2})$ and $C_1(\frac{\pi}{2})$. The value of v influences the sizes of the Cs, which is why the trajectories seem to approach the x axis at a larger y for larger values of v in Fig. 3.30. It is seen that the action reduction on increasing v is much larger than on increasing D_θ.

3.5.4 Dependence on parameters

Unlike the harmonic potential, gradient descent inside C_1 is only a small part of the total path. Thus, the issue of trajectories leaving C_1 at the wrong point is a lot less important here. The general trend of higher α allowing a greater deviation from initial condition is still true. The GDA is also unstable for α outside the rough range of $(0.01, 0.12)$, and the largest possible value is in general better.

For reasonable initial guesses and remaining parameters, $\Delta\tau$ only affects the rate of convergence. In some cases, there is slight variation in the action of the trajectory to which it converges. For bad initial guesses (for example, a θ that varies a lot for $D_\theta \approx 0.1$), the value of $\Delta\tau$ can affect convergence. In general, a $\Delta\tau$ in the range (0.01,0.05) works best.

Increasing the number of discretization points beyond 400-500 does not have a noticeable effect and decreases speed so it is fixed at 400 or 500.

The GMAM does not converge for D_θ larger than $O(10)$, due to k_θ or θ blowing up. This is to be expected because of the linear dependence of $\dot{\theta} = D_\theta k_\theta$ on D_θ. In the update equations, the contribution of D_θ is of the form

$$\frac{\Delta\tau\Delta s D_\theta}{\Delta s + \Delta\tau} \tag{3.59}$$

Thus, to make the increase per step constant, it is advantageous to decrease either $\Delta\tau$ or Δs (assuming that this is the reason for the instability). The former makes convergence slow and the latter makes updates slow.

3.5.5 Dependence on initial condition

As with most path based optimization techniques the choice of initial condition is important especially because the minimum action path is highly degenerate. For the trajectories in Fig. 3.32, the initial guess for x, y is linear in s between initial and final points with some noise added. The guess for θ is a linear function of s between different values of θ_i and θ_f depending on the boundary conditions used.

This initial path is first generated with 5-10 points and some Gaussian noise with mean 0 and standard deviation 0.01-0.1 is added. Then, using the parametric spline interpolation a reasonable initial guess is formed. The smoothness of the guess can be adjusted with the order of interpolation.

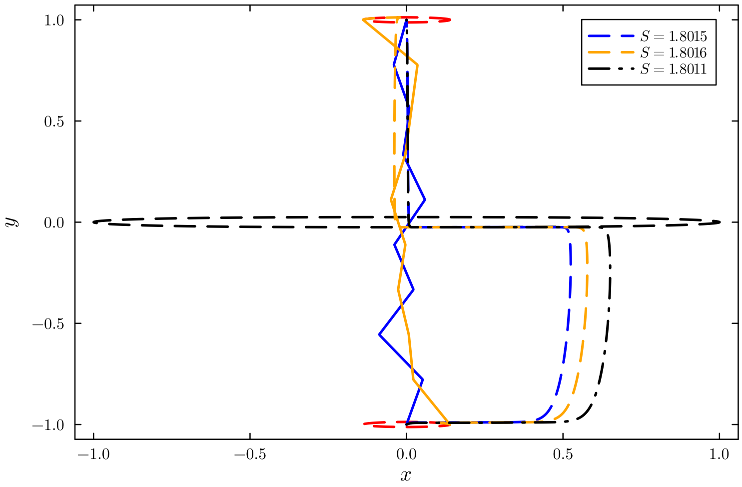

(a) Different initial conditions used

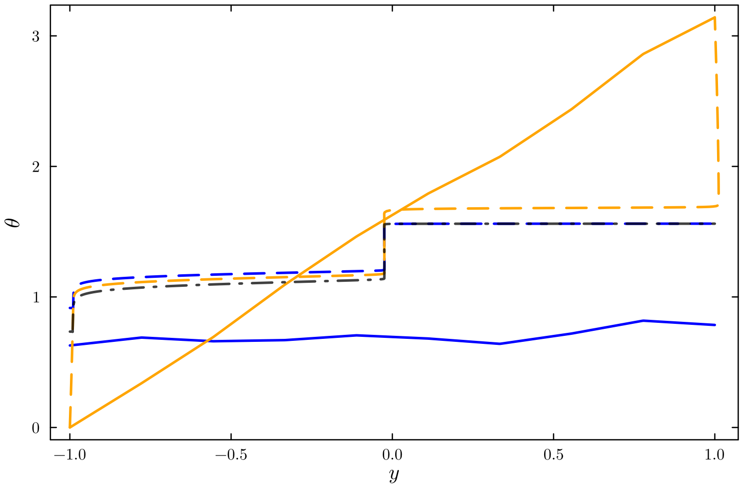

(b) The solid lines are the initial conditions and the dashed lines are the solution trajectories. The black trajectory is from Fig. 3.28

Figure 3.32: Dependence on initial conditions for $D_\theta = 2.5$ and $v = 0.1$.

For the figures above, the initial guesses are generated with a linear interpolation. For the orange trajectory which goes from $C_1(0)$ to $C_3(\pi)$, θ is fixed at the boundaries to be 0 and π respectively. The different trajectories have actions that are different by only $O(10^{-3})$. The symmetric action is 1.0836. Since the algorithm is very sensitive to initial conditions here, it means that the GMAM is not sufficiently precise to recognize action differences of 10^{-3}.

When the asymmetric action differs by about 10^{-2}, most initial conditions that are not the symmetric trajectory converge to the same solution.

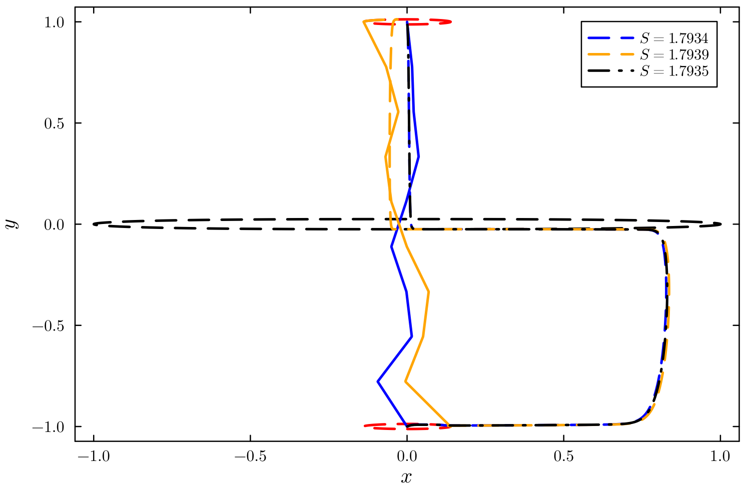

(a) Different initial conditions and solutions. The black trajectory is the solution from Fig. 3.28

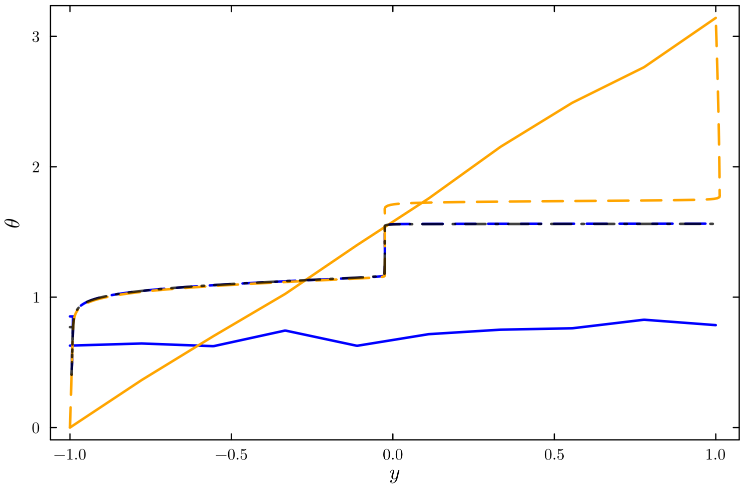

(b) Comparison of θ for different initial conditions

Figure 3.33: Dependence on initial conditions for $D_\theta = 4.5$ and $v = 0.1$.

The symmetric action is 1.8036 so the difference is approximately 10^{-2}. Thus, we consider an asymmetric trajectory significant if its action is lower than the symmetric one by at least 10^{-2}.

3.5.6 Comparison with the Ritz method

As mentioned in Section 3.2, the deviations of GMAM trajectories from solutions to Hamilton's equations is small but much larger than floating point accuracy. For the harmonic potential, we could compare with the collocation method to verify solutions. For the double well, the results are compared to solutions from the Ritz method[25] obtained by Dr. Rafael Díaz. The Ritz method works by using a polynomial basis for the paths. Using a quadrature rule, the Lagrangian can be obtained as a function of the weights of different polynomials in the basis. This works quite well with GWN but can not be extended to include shot noise. The action values and trajectories from the GMAM are compared to those obtained by the Ritz method and there is reasonable agreement. An example is given below.

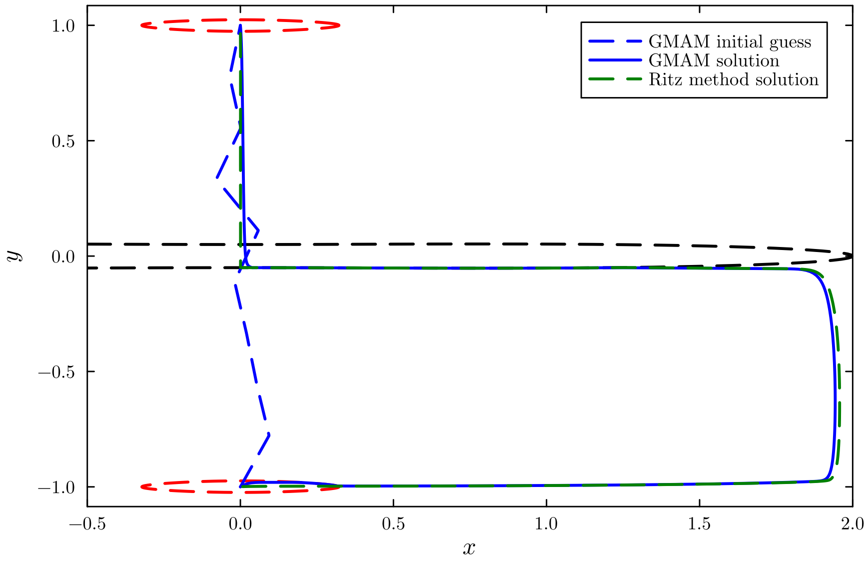

(a) Compariaon of solutions from the GMAM and Ritz method

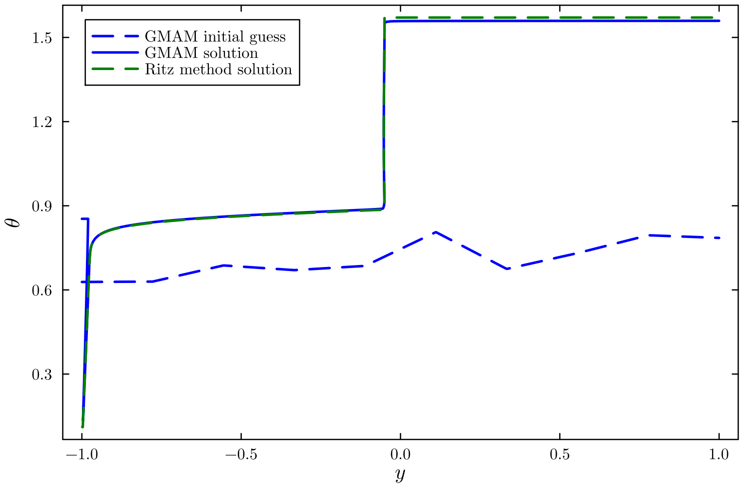

(b) Comparison of θ

Figure 3.34: Comparison of solutions for $v = 0.2, D_\theta = 0.5$. The actions are 1.4711 for the GMAM and 1.4721 which is well within the margin of error

Chapter 4

Conclusion and Outlook

We have studied the escape behaviour of 2-d Run and Tumble particles from different types of confining potentials and in the presence of different types of angular noise using the MSR formalism. For ABPs without any run and tumble motion, we replicate the results seen in [10] and [15] using the MSR formalism. For type-1 shot noise where the moment generating function is finite, we see an exponential speed up of the escape rate compared to the effective Gaussian noise approximation but the speed-up is considerably less efficient than what was observed in [14] when the shot noise acts directly on the positional degrees of freedom. For type-2 shot noise where the moment generating function is defined on a finite interval with singularities at the boundaries, we describe with analytical results the behavior of the trajectory before, during and after a jump in the self propulsion direction in the persistent limit. We also calculate the Lagrangian in the persistent limit and use it to find the cost of a jump in θ. Unfortunately, we could not verify our results numerically and the reason for the discrepancy between numerics and analytical predictions is to be investigated. We also find action minimizing trajectories taking infinite time with an implementation of a GAD-GMAM method described in [21] for an elliptic potential and double well. For the elliptic potential, we confirm the finite time approximations obtained by the collocation method and for the double well we briefly describe the phenomena of symmetry breaking by persistence where the preferred transition pathway shows a discontinuous jump on changing the persistence time and self propulsion speed. We also discuss details relating to parameter choice and dependence on initial condition for the GMAM.

There are several possible directions of future work from this thesis. As mentioned before, numerical verification of the persistent limit of type-2 noise is still pending. Moreover, only the double persistent limit i.e. $\lambda \to 0$ and $D_\theta \to 0$ were considered in detail. The limit $\lambda \to 0$ with $D_\theta \to \infty$ or remaining finite are interesting directions to explore. Finally, the effect of type-3 noise is still an open question. Even though our GMAM implementation is capable of handling all 3 types of shot noise in principle, we have not tested it with $\lambda > 0$. Since path based optimization can be capable of handling the finite λ jumps seen in type-3 noises, it could be fruitful to test the GMAM with type-3 noise.

Furthermore, the MSR formalism is well suited for studying non-equilibrium phase transitions due to activity. The dependence of the minimal action for a transition between two metastable states (or the quasi-potential difference between them[21]) on control parameters can result in sharp changes in the preferred transition pathway. Although we have briefly discussed an example in Section 3.5, the effect of non-Gaussian noise on the transition has not been studied yet. Other potential landscapes could also show novel effects of activity on the preferred transition pathway.

While we have only studied the escape of a single particle, collective effects can influence escape rates of interacting Brownian particles. The generalized Kramer's form for the escape rate of multiple interacting passive Brownian particles[26] suggests that adding activity might show interesting behavior. Narrow escape is also a related but distinctly different problem that can be tackled. In narrow escape problems, the confinement is not due to a smooth potential but a hard boundary with a narrow pore through which the particle must escape[27].

Appendices

Appendix A

The MSR action

We use the MSR path integral formalism to derive path probabilities upto a normalization constant[28]. The general strategy is to discretize the path into independent increments and write down the probability of all such increments given the noise properties. Here, we will use $\mathbf{r}$ to refer to the positional degrees of freedom (x, y) and θ to refer to the angular degree of freedom. $\mathbf{q}$ will refer to (x, y, θ). We will use an Itô discretization scheme for the positional and angular degree of freedom

$$\dot{\mathbf{r}} = -\nabla V(\mathbf{r}) + v\hat{\theta} + \xi_{\mathbf{r}} \implies \mathbf{r}_{s+1} - \mathbf{r}_s = -\nabla V(\mathbf{r}_i)\Delta t + v\hat{\theta}_i \Delta t + \xi^s_{\mathbf{r}}(\Delta t) \tag{A.1}$$

$$\dot{\theta} = \xi_{PSN} + \xi_{GWN} \implies \theta_{s+1} - \theta_i = \xi^i_{PSN}(\Delta t) + \xi^i_{GWN}(\Delta t) \tag{A.2}$$

Here, for convenience the vector $\hat{\theta}$ is defined as

$$\hat{\theta} = \begin{bmatrix} \cos\theta \\ \sin\theta \end{bmatrix} \tag{A.3}$$

The index s runs from 1 to $n-1$ where $\mathbf{r}_1 = \mathbf{r}_i$ and $\mathbf{r}_n = \mathbf{r}_f$, the initial and final points. Thus, the equations describe the update procedure for the indices $s = 1$ to $n-1$. For a given final time t_f, $\Delta t = \frac{t_f}{n-1}$. The term $\xi^s_{\mathbf{r}}(\Delta t)$ is the noise increment between interval s and $s+1$ for the positional coordinates. Similarly, the other terms in (A.2) refer to the angular noise increments. For the Gaussian components, this is easy to calculate.

$$\xi^s_{\mathbf{r}}(\Delta t) = \int_{s\Delta t}^{(s+1)\Delta t} \xi_{\mathbf{r}}(t)dt \sim \mathcal{N}(0, \tilde{D}\Delta t) \tag{A.4}$$

For the shot noise, this is harder to calculate in general, but since we will be taking the limit $\Delta t \to 0$, we can make the assumption that only one kick occurs between $s\Delta t$ and $(s+1)\Delta t$ since the probability of multiple kicks go as $O(\Delta t^2)$. Thus for small Δt, the PSN increments are distributed as

$$\mathbb{P}\left[\xi^i_{PSN}(\Delta t) = y\right] = \mathbb{P}\left[\int_{s\Delta t}^{(s+1)\Delta t} \xi^i_{PSN}(t)dt = y\right] \tag{A.5}$$

$$= \tilde{\lambda}\Delta t\rho(ay) + \delta(y)(1 - \tilde{\lambda}\Delta t) \tag{A.6}$$

Since we have the probabilities for the independent increments, we can use this to write down the discretized path probability. Fix a discretized path $\mathbf{q}$. To find the probability of this path, we need to integrate over all noise realizations ξ that satisfy (A.1) and (A.2) for that particular $\mathbf{q}$. Thus, the consistency condition for the increments $\mathbf{q}_{s+1} - \mathbf{q}_i$ that ξ needs to satisfy is that

$$\xi^s_{\mathbf{r}}(\Delta t) = \mathbf{r}_{s+1} - \mathbf{r}_s + \nabla V(\mathbf{r}_i)\Delta t - v\hat{\theta}_i\Delta t \tag{A.7}$$

$$\xi^i_{PSN}(\Delta t) + \xi^i_{GWN}(\Delta t) = \theta_{s+1} - \theta_i \tag{A.8}$$

The right-hand sides of the equations above will be denoted by $\mathbf{\Delta}^i_{\mathbf{r}}$ and Δ^i_θ respectively. Since the increments are independent, the total path probability can be written as follows:

$$\mathbb{P}[\mathbf{q}] = \prod_{s=1}^{n-1} \mathbb{P}(\mathbf{q}_{s+1} - \mathbf{q}_s) \tag{A.9}$$

$$= \prod_{s=1}^{n-1} \mathbb{P}(\xi^s_{\mathbf{r}}(\Delta t) = \mathbf{\Delta}^s_{\mathbf{r}})\mathbb{P}(\xi^s_{GWN}(\Delta t) + \xi^s_{PSN}(\Delta t) = \Delta^s_\theta)J(\mathbf{q}_i) \tag{A.10}$$

Where J is the Jacobian that accounts for the change of variables from $\mathbf{q}$ to ξ. For the Itô discretization scheme, $J = 1$[28]. The probabilities on the right-hand side can be rewritten as an average of a δ function

$$\mathbb{P}[\mathbf{q}] = \prod_{s=1}^{n-1} \left\langle \delta^2(\mathbf{\Delta}^s_{\mathbf{r}} - \xi^s_{\mathbf{r}}(\Delta t))\right\rangle \left\langle \delta(\Delta^s_\theta - \xi^i_\theta(\Delta t))\right\rangle_\xi \tag{A.11}$$

$$= \prod_{s=1}^{n-1} \frac{1}{(2\pi)^3} \left\langle \int \exp\left[-i\mathbf{g}^s \cdot (\mathbf{\Delta}^s_q - \xi^s(\Delta t))\right] \mathrm{d}\mathbf{g}^s \right\rangle_\xi \tag{A.12}$$

$$= \prod_{s=1}^{n-1} \frac{1}{(2\pi)^3} \int \exp\left(-i\mathbf{g}^s \cdot \mathbf{\Delta_q}^s\right) \left\langle \exp\left[i\mathbf{g}^s \cdot \xi^s_{\mathbf{q}}\right]\right\rangle_\xi \mathrm{d}\mathbf{g}_i \tag{A.13}$$

The average is just the characteristic function of $\xi^s_{\mathbf{q}}(\Delta t)$ evaluated at $\mathbf{g}^s$. Since $\xi^s_{\mathbf{r}}(\Delta t) \sim \mathcal{N}(0, \tilde{D}\Delta t)$, its characteristic function is simply

$$\exp\left(-\frac{\tilde{D}\Delta t \mathbf{g}^{\mathbf{s}}_{\mathbf{r}} \cdot \mathbf{g}^{\mathbf{s}}_{\mathbf{r}}}{2}\right) \tag{A.14}$$

Since the GWN and PSN on θ are independent, the characteristic function of their sum is just the product of their individual characteristic functions. The GWN portion again has the form $\exp(-\frac{D_\theta \Delta t g_\theta^2}{2})$. For the PSN term, it can be calculated as

$$\begin{aligned}
\langle \exp(i\tilde{a}g^s_\theta \xi^s_{PSN})\rangle_{\xi_{PSN}} &= (1-\tilde{\lambda}\Delta t) + \tilde{\lambda}\Delta t \left\langle \exp(i g_\theta x)\right\rangle_\rho \qquad &(A.15)\\
&= 1 + \tilde{\lambda}\Delta t \left\langle \exp(i g^s_\theta x) - x\right\rangle_\rho &(A.16)\\
&\approx \exp\left[\tilde{\lambda}\Delta t \left\langle \exp(i\tilde{a} g^s_\theta x) - x\right\rangle_\rho\right] &(A.17)\\
&= \exp[\tilde{\lambda}\Delta t \phi(i\tilde{a}g^s_\theta)] &(A.18)
\end{aligned}$$

The approximation is again valid for small Δt only as it follows from (A.6). Now we plug these values for the characteristic function back into (A.13) and take the $\Delta t \to 0$ limit keeping $t_f = \Delta t(n-1)$ constant.

$$\mathbb{P}[\mathbf{q}] = \prod_{s=1}^{n-1}\int \exp\left(-i\mathbf{g}^s_\mathbf{q}\cdot\boldsymbol{\Delta}^s_\mathbf{q} - \frac{\Delta t(\mathbf{g}^s_\mathbf{q})^T\tilde{\mathbf{D}}_\mathbf{q}\mathbf{g}^s_\mathbf{q}}{2} + \tilde{\lambda}\Delta t\phi(i\tilde{a}g^s_\theta)\right)\frac{\mathrm{d}\mathbf{g}^s_\mathbf{q}}{(2\pi)^3} \tag{A.19}$$

$$= \int \exp\left(\sum_{i=1}^{n} -i\mathbf{g}^s_\mathbf{q}\cdot\boldsymbol{\Delta}^s_\mathbf{q} - \frac{\Delta t(\mathbf{g}^s_\mathbf{q})^T\tilde{\mathbf{D}}_\mathbf{q}\mathbf{g}^s_\mathbf{q}}{2} + \tilde{\lambda}\phi(i\tilde{a}g^s_\theta)\right)\mathrm{d}\left(\frac{\mathbf{g}_\mathbf{q}}{(2\pi)^3}\right)^{n-1} \tag{A.20}$$

$$\to \int \exp\left(\int\left[-i\mathbf{g}_\mathbf{q}\cdot\dot{\mathbf{q}} - i\mathbf{g}_\mathbf{r}\cdot\nabla_\mathbf{r}V_{eff}(\mathbf{q}) - \frac{\mathbf{g}^T_\mathbf{q}\tilde{\mathbf{D}}_\mathbf{q}\mathbf{g}_\mathbf{q}}{2} + \tilde{\lambda}\phi(i\tilde{a}g_\theta)\right]\mathrm{d}t\right)\mathcal{D}\left[\frac{\mathbf{g}}{2\pi}\right] \tag{A.21}$$

In the $\Delta t \to 0$, limit we obtain the probability for a path $\mathbf{q}(t)$ as a path integral over the functions $\mathbf{g}(t)$ where $t \in [0, t_f]$. To apply the large deviation approach, we make the path probability sharply peaked about a maximum value such that deviations from this most likely escape path are exponentially unlikely. Physically, we do this by looking at the weak noise regime, where the strength of the noise is vanishing. For the Gaussian components, the obvious choice is to send $\tilde{D} \to 0$. This is done as

$$\tilde{D} = \varepsilon D \qquad \varepsilon \to 0 \tag{A.22}$$

To make the exponential sharply peaked and of the form $\exp(-\frac{1}{\varepsilon})$, $\mathbf{g}_\mathbf{q}$ is rescaled as $\frac{\mathbf{g}_\mathbf{q}}{\varepsilon}$. For $\lambda = 0$, the action is thus of the form

$$\int \frac{1}{\varepsilon}\left(-i\mathbf{g}_\mathbf{q}\cdot\dot{\mathbf{q}} - i\mathbf{g}_\mathbf{r}\cdot\nabla_\mathbf{r}V_{eff}(\mathbf{q}) - \frac{\mathbf{g}^T_\mathbf{q}\mathbf{D}_\mathbf{q}\mathbf{g}_\mathbf{q}}{2}\right) \tag{A.23}$$

For the PSN, the variance is $\tilde{\lambda}\tilde{a}^2$ which depends on two parameters. The expected physics changes based on how they are individually changed to reach the limit. Since

ρ is symmetric, the Taylor expansion of ϕ is of the form

$$\tilde{\lambda}\phi(\tilde{a}x) = \tilde{\lambda}(b_2\tilde{a}^2x^2 + b_4\tilde{a}^4x^4 + \dots) \tag{A.24}$$

It is necessary that $\tilde{a} \to 0$ faster than ε as otherwise, $\tilde{\lambda}\phi(\tilde{a}\frac{g_\theta}{\varepsilon})$ does not scale as $\frac{1}{\varepsilon}$. Since the non-Gaussian behaviour is captured in ϕ, we would like all terms in the expansion to remain non-zero in the weak noise limit. Thus, the scalings should ensure that $\tilde{\lambda}(\tilde{a}\frac{g}{\varepsilon})^n \geq 0 \ \forall \ n > 0$. An easy way to satisfy this and ensure the weak noise condition is if $\tilde{a} = a\varepsilon$ and $\tilde{\lambda} = \frac{\lambda}{\varepsilon}$. It can be shown that this is the unique scaling that allows this, for λ and a that go to zero exponentially in ε. In terms of the new noise strength variables, the path probability and its saddle point approximation can be written as

$$\mathbb{P}[\mathbf{q}] = \int \exp\left[\int -\frac{1}{\varepsilon}\left(i\mathbf{g_q}\cdot\dot{\mathbf{q}} + i\mathbf{g_r}\cdot\nabla_\mathbf{r}V_{eff}(\mathbf{q}) + \frac{\mathbf{g_q}^T\mathbf{D_q}\mathbf{g_q}}{2} - \lambda\phi(iag_\theta)\right)\mathrm{d}t\right]\mathcal{D}\left[\frac{\mathbf{g_q}}{2\pi}\right] \tag{A.25}$$

$$\approx \exp\left[-\frac{1}{\varepsilon}\int \min_{\mathbf{g_q}}\left(i\mathbf{g_q}\cdot\dot{\mathbf{q}} + i\mathbf{g_r}\cdot\nabla_\mathbf{r}V_{eff}(\mathbf{q}) + \frac{\mathbf{g_q}^T\mathbf{D_q}\mathbf{g_q}}{2} - \lambda\phi(iag_\theta)\right)\mathrm{d}t\right] \tag{A.26}$$

$$= \exp\left[\int \max_{\mathbf{k_q}} -\frac{1}{\varepsilon}\left(\mathbf{k_q}\cdot\dot{\mathbf{q}} + \mathbf{k_r}\cdot\nabla_\mathbf{r}V_{eff}(\mathbf{q}) - \frac{\mathbf{k_q}^T\mathbf{D_q}\mathbf{k_q}}{2} - \lambda\phi(ak_\theta)\right)\mathrm{d}t\right] \tag{A.27}$$

In the last step, the variables transformation $\mathbf{k_q} = i\mathbf{g_q}$ has been made. Notice that the minimum in $\mathbf{g_q}$ happens on the imaginary axis since the minimizing point satisfies

$$i\mathbf{q} + i\nabla_\mathbf{r}V_{eff}(\mathbf{q}) - \lambda ai\phi(aig_\theta) = -\frac{\mathbf{g_q}^T\mathbf{D_q}\mathbf{g_q}}{2} \tag{A.28}$$

and the LHS, removing the factor of i, is always real. Thus, the maximizing value of $\mathbf{k_q}$ is real valued. This allows us to interpret $\mathbf{k_q}$ as the momenta conjugate to $\mathbf{q}$. Thus, the probability density is concentrated on a path that minimizes the action

$$S(\mathbf{q},\dot{\mathbf{q}}) = \int_0^{t_f} \max_{\mathbf{k_q}}\left(\mathbf{k_q}\cdot\dot{\mathbf{q}} + \mathbf{k_r}\cdot\nabla_\mathbf{r}V_{eff}(\mathbf{q}) - \frac{\mathbf{k_q}^T\mathbf{D_q}\mathbf{k_q}}{2} - \lambda\phi(ak_\theta)\right)\mathrm{d}t \tag{A.29}$$

$$= \int_0^{t_f} \max_{\mathbf{k_q}}\left(\mathbf{k_q}\cdot\dot{\mathbf{q}} - \mathcal{H}(\mathbf{q},\mathbf{k_q})\right)\mathrm{d}t \tag{A.30}$$

$$= \int_0^{t_f} \mathcal{L}(\mathbf{q},\dot{\mathbf{q}})\mathrm{d}t \tag{A.31}$$

Since we are interested in escape paths between fixed points $\mathbf{r}_i$ and $\mathbf{r}_f$, we minimize the action over paths with boundaries fixed at these values. However, the self propulsion angle is free at the boundaries. The third boundary condition to fix the minimum action path is derived from the fact that the action still has to be stationary in θ. The stationary action condition for θ is

$$\begin{aligned} \delta S &= \int_0^{t_f} \left(\frac{\partial \mathcal{L}}{\partial \theta} \delta\theta + \frac{\partial \mathcal{L}}{\partial \dot{\theta}} \delta\dot{\theta} \right) && \text{(A.32)} \\ &= \int_0^{t_f} \left[\frac{\partial \mathcal{L}}{\partial \theta} \delta\theta + \frac{\mathrm{d}}{\mathrm{d}t} \left(\frac{\partial \mathcal{L}}{\partial \dot{\theta}} \delta\theta \right) - \frac{\mathrm{d}}{\mathrm{d}t} \left(\frac{\partial \mathcal{L}}{\partial \dot{\theta}} \right) \right] && \text{(A.33)} \\ &= \int_0^{t_f} \left[\frac{\partial \mathcal{L}}{\partial \theta} - \frac{\mathrm{d}}{\mathrm{dt}} \left(\frac{\partial \mathcal{L}}{\partial \dot{\theta}} \right) \delta\theta \right] \delta\theta \mathrm{d}t + \left[\frac{\partial \mathcal{L}}{\partial \dot{\theta}} \delta\theta \right]_0^{t_f} && \text{(A.34)} \end{aligned}$$

To remove the boundary term, we set $\frac{\partial L}{\partial \dot{\theta}} = k_\theta = 0$ at both ends.

Bibliography

1. Romanczuk, P., Bär, M., Ebeling, W., Lindner, B. & Schimansky-Geier, L. Active Brownian Particles: From Individual to Collective Stochastic Dynamics. *The European Physical Journal Special Topics* **202,** 1–162 (Mar. 2012).
2. Solon, A. P., Cates, M. E. & Tailleur, J. Active Brownian Particles and Run-and-Tumble Particles: A Comparative Study. *The European Physical Journal Special Topics* **224,** 1231–1262 (July 2015).
3. Bechinger, C. *et al.* Active Particles in Complex and Crowded Environments. *Reviews of Modern Physics* **88,** 045006 (Nov. 23, 2016).
4. Cates, M. E. & Tailleur, J. Motility-Induced Phase Separation. *Annual Review of Condensed Matter Physics* **6,** 219–244 (Mar. 1, 2015).
5. Kramers, H. Brownian Motion in a Field of Force and the Diffusion Model of Chemical Reactions. *Physica* **7,** 284–304 (Apr. 1940).
6. Forgoston, E. & Moore, R. O. A Primer on Noise-Induced Transitions in Applied Dynamical Systems. *SIAM Review* **60,** 969–1009 (Jan. 2018).
7. Guéneau, M., Majumdar, S. N. & Schehr, G. Run-and-Tumble Particle in One-Dimensional Potentials: Mean First-Passage Time and Applications. *Physical Review E* **111,** 014144 (Jan. 22, 2025).
8. Santra, I., Basu, U. & Sabhapandit, S. Run-and-Tumble Particles in Two Dimensions: Marginal Position Distributions. *Physical Review E* **101,** 062120 (June 15, 2020).
9. Kiechl, T., Franosch, T. & Caraglio, M. Transition-Path Sampling for Run-and-Tumble Particles. *Physical Review E* **110,** 054121 (Nov. 18, 2024).
10. Woillez, E., Zhao, Y., Kafri, Y., Lecomte, V. & Tailleur, J. Activated Escape of a Self-Propelled Particle from a Metastable State. *Physical Review Letters* **122,** 258001 (June 28, 2019).
11. Caraglio, M. *Two-Dimensional Active Brownian Particles Crossing a Parabolic Barrier: Transition-Path Times, Survival Probability, and First-Passage Time* version 1. `https://arxiv.org/abs/2410.07226` (2025). Pre-published.
12. Sharma, A., Wittmann, R. & Brader, J. M. Escape Rate of Active Particles in the Effective Equilibrium Approach. *Physical Review E* **95,** 012115 (Jan. 10, 2017).

13. Allen, R. J., Valeriani, C. & Rein Ten Wolde, P. Forward Flux Sampling for Rare Event Simulations. *Journal of Physics: Condensed Matter* **21,** 463102 (Nov. 18, 2009).
14. Baule, A. & Sollich, P. Exponential Increase of Transition Rates in Metastable Systems Driven by Non-Gaussian Noise. *Scientific Reports* **13,** 3853 (Mar. 8, 2023).
15. Peters, L. *Escape Rates of Active Brownian Particles in an Elliptic Potential* Internship Report (Georg-August-Universität Göttingen, Göttingen, Sept. 2023).
16. Touchette, H. The Large Deviation Approach to Statistical Mechanics. *Physics Reports* **478,** 1–69 (July 2009).
17. Freidlin, M. I. & Wentzell, A. D. *Random Perturbations of Dynamical Systems* (Springer Berlin Heidelberg, Berlin, Heidelberg, 2012).
18. Jensen, R. V. Functional Integral Approach to Classical Statistical Dynamics. *Journal of Statistical Physics* **25,** 183–210 (June 1981).
19. Hanggi, P. Escape from a Metastable State. *Journal of Statistical Physics* **42,** 105–148 (Jan. 1986).
20. Rackauckas, C. & Nie, Q. Differentialequations.jl–a performant and feature-rich ecosystem for solving differential equations in julia. *Journal of Open Research Software* **5,** 15 (2017).
21. Zakine, R. & Vanden-Eijnden, E. Minimum-Action Method for Nonequilibrium Phase Transitions. *Physical Review X* **13,** 041044 (Dec. 7, 2023).
22. E, W., Ren, W. & Vanden-Eijnden, E. String Method for the Study of Rare Events. *Physical Review B* **66,** 052301 (Aug. 12, 2002).
23. Cugliandolo, L. F. & Lecomte, V. Rules of Calculus in the Path Integral Representation of White Noise Langevin Equations: The Onsager–Machlup Approach. *Journal of Physics A: Mathematical and Theoretical* **50,** 345001 (Aug. 25, 2017).
24. Heymann, M. & Vanden-Eijnden, E. The Geometric Minimum Action Method: A Least Action Principle on the Space of Curves. *Communications on Pure and Applied Mathematics* **61,** 1052–1117 (Aug. 2008).
25. Kikuchi, L., Singh, R., Cates, M. E. & Adhikari, R. Ritz Method for Transition Paths and Quasipotentials of Rare Diffusive Events. *Physical Review Research* **2,** 033208 (Aug. 6, 2020).
26. Kumar, V., Pal, A. & Shpielberg, O. Arrhenius Law for Interacting Diffusive Systems. *Physical Review E* **109,** L032101 (Mar. 6, 2024).
27. Paoluzzi, M., Angelani, L. & Puglisi, A. Narrow-Escape Time and Sorting of Active Particles in Circular Domains. *Physical Review E* **102,** 042617 (Oct. 27, 2020).

28. Hertz, J. A., Roudi, Y. & Sollich, P. Path Integral Methods for the Dynamics of Stochastic and Disordered Systems. *Journal of Physics A: Mathematical and Theoretical* **50,** 033001 (Jan. 20, 2017).